



Universiteit
Leiden
The Netherlands

CORINOS. I. JWST/MIRI spectroscopy and imaging of a class 0 protostar IRAS 15398-3359

Yang, Y.-L.; Green, J.D.; Pontoppidan, K.M.; Bergner, J.B.; Cleeves, L.I.; Evans, N.J.; ... ;
Dishoeck, E.F. van

Citation

Yang, Y. -L., Green, J. D., Pontoppidan, K. M., Bergner, J. B., Cleeves, L. I., Evans, N. J., ...
Dishoeck, E. F. van. (2022). CORINOS. I. JWST/MIRI spectroscopy and imaging of a class 0
protostar IRAS 15398-3359. *Astrophysical Journal Letters*, 941(1).
doi:10.3847/2041-8213/aca289















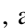

Version: Publisher's Version
License: [Creative Commons CC BY 4.0 license](https://creativecommons.org/licenses/by/4.0/)
Downloaded from: <https://hdl.handle.net/1887/3561258>

Note: To cite this publication please use the final published version (if applicable).



CrossMark

CORINOS. I. JWST/MIRI Spectroscopy and Imaging of a Class 0 Protostar IRAS 15398–3359

Yao-Lun Yang^{1,2} , Joel D. Green³ , Klaus M. Pontoppidan³ , Jennifer B. Bergner⁴ , L. Ilseore Cleaves² ,
Neal J. Evans II⁵ , Robin T. Garrod⁶ , Mihwa Jin^{7,8} , Chul Hwan Kim⁹ , Jaeyeong Kim¹⁰ , Jeong-Eun Lee⁹ ,
Nami Sakai¹ , Christopher N. Shingledecker¹¹ , Brielle Shope¹² , John J. Tobin¹³ , and Ewine F. van Dishoeck^{14,15} 

¹RIKEN Cluster for Pioneering Research, Wako-shi, Saitama, 351-0198, Japan; yaolunyang.astro@gmail.com

²Department of Astronomy, University of Virginia, Charlottesville, VA 22904, USA

³Space Telescope Science Institute, Baltimore, 3700 San Martin Dr., MD 21218, USA

⁴University of Chicago Department of the Geophysical Sciences, Chicago, IL 60637, USA¹⁶

⁵Department of Astronomy, The University of Texas at Austin, Austin, TX 78712, USA

⁶Departments of Chemistry and Astronomy, University of Virginia, Charlottesville, VA 22904, USA

⁷Astrochemistry Laboratory, Code 691, NASA Goddard Space Flight Center, Greenbelt, MD 20771, USA

⁸Department of Physics, Catholic University of America, Washington, DC 20064, USA

⁹Department of Physics and Astronomy, Seoul National University, 1 Gwanak-ro, Gwanak-gu, Seoul 08826, Republic of Korea

¹⁰Korea Astronomy and Space Science Institute, 776 Daedeok-daero, Yuseong-gu Daejeon 34055, Republic of Korea

¹¹Department of Physics and Astronomy, Benedictine College, Atchison, KS 66002, USA

¹²Department of Chemistry, University of Virginia, 409 McCormick Rd., Charlottesville, VA, 22904, USA

¹³National Radio Astronomy Observatory, 520 Edgemont Rd., Charlottesville, VA 22903, USA

¹⁴Leiden Observatory, Leiden University, Leiden, Netherlands

¹⁵Max Planck Institute for Extraterrestrial Physics, Garching, Germany

Received 2022 August 21; revised 2022 November 6; accepted 2022 November 10; published 2022 December 12

Abstract

The origin of complex organic molecules (COMs) in young Class 0 protostars has been one of the major questions in astrochemistry and star formation. While COMs are thought to form on icy dust grains via gas-grain chemistry, observational constraints on their formation pathways have been limited to gas-phase detection. Sensitive mid-infrared spectroscopy with JWST enables unprecedented investigation of COM formation by measuring their ice absorption features. Mid-infrared emission from disks and outflows provide complementary constraints on the protostellar systems. We present an overview of JWST/Mid-Infrared Instrument (MIRI) Medium Resolution Spectroscopy (MRS) and imaging of a young Class 0 protostar, IRAS 15398–3359, and identify several major solid-state absorption features in the 4.9–28 μm wavelength range. These can be attributed to common ice species, such as H_2O , CH_3OH , NH_3 , and CH_4 , and may have contributions from more complex organic species, such as $\text{C}_2\text{H}_5\text{OH}$ and CH_3CHO . In addition to ice features, the MRS spectra show many weaker emission lines at 6–8 μm , which are due to warm CO gas and water vapor, possibly from a young embedded disk previously unseen. Finally, we detect emission lines from [Fe II], [Ne II], [S I], and H_2 , tracing a bipolar jet and outflow cavities. MIRI imaging serendipitously covers the southwestern (blueshifted) outflow lobe of IRAS 15398–3359, showing four shell-like structures similar to the outflows traced by molecular emission at submillimeter wavelengths. This overview analysis highlights the vast potential of JWST/MIRI observations and previews scientific discoveries in the coming years.

Unified Astronomy Thesaurus concepts: Astrochemistry (75); Star formation (1569); Protostars (1302); Stellar winds (1636); Stellar jets (1607); Complex organic molecules (2256)

1. Introduction

In recent years, complex organic molecules (COMs), first detected in high-mass cores (Sutton et al. 1985; Blake et al. 1986, 1987), have been routinely detected in the gas phase in low-mass protostellar cores, suggesting extensive chemical evolution at the early stage of low-mass star formation (e.g., van Dishoeck et al. 1995; Ceccarelli et al. 2007; Jørgensen et al. 2020; Ceccarelli et al. 2022). These low-mass cores are often called “hot corinos” (Cazaux et al. 2003; Bottinelli et al. 2004; Ceccarelli 2004). The COMs, commonly defined as organic molecules with six or more atoms (Herbst & van Dishoeck 2009),

could be the precursors of prebiotic molecules (e.g., Jiménez-Serra et al. 2020). Solar system objects, such as comets, also show abundant COMs (Altwegg et al. 2019); and in some cases, the COM abundances match those measured in protostellar cores, hinting at a chemical connection from protostars to planetary systems (Bockelée-Morvan et al. 2000; Drozdovskaya et al. 2019; Bianchi et al. 2019a). Thus, the origin of the rich organic chemistry in the protostellar stage is of great interest in characterizing the chemical environment of planet-forming disks.

Current models predict that a combination of gas-phase and ice-phase processes (i.e., “gas-grain chemistry”) is responsible for COM formation in protostellar environments (e.g., Garrod et al. 2008; Taquet et al. 2014; Lu et al. 2018; Quénard et al. 2018; Soma et al. 2018; Aikawa et al. 2020). These models generally require a warm-up phase during which the elevated temperature enables efficient reactions via diffusion. In addition to the formation of COMs in the ice phase, gas-phase

¹⁶ NASA Sagan Fellow.



Original content from this work may be used under the terms of the [Creative Commons Attribution 4.0 licence](https://creativecommons.org/licenses/by/4.0/). Any further distribution of this work must maintain attribution to the author(s) and the title of the work, journal citation and DOI.

reactions following sublimation of simpler ice molecules may contribute to the production of several COMs (Balucani et al. 2015; Skouteris et al. 2018; Vazart et al. 2020). Laboratory experiments show that COMs can also be formed on icy surfaces even at low temperature (Chuang et al. 2016; Fedoseev et al. 2017; Bergner et al. 2019b; Qasim et al. 2019). Extended distributions of COMs in cold prestellar cores further suggest ongoing formation of COMs in the ice phase (Jimenez-Serra et al. 2016; Vasyunin et al. 2017; Scibelli & Shirley 2020; Punanova et al. 2022). To reconcile the presence of COMs at low temperature, a modified gas-grain chemical model that includes nondiffusive reactions at low temperature has been proposed (Jin & Garrod 2020; Garrod et al. 2022).

Recent surveys show that gas-phase COM emission is common, but not ubiquitous, around Class 0/I protostars, with detection fractions around half (Bergner et al. 2019a; Bianchi et al. 2019b; Belloche et al. 2020; van Gelder et al. 2020; Nazari et al. 2021; Yang et al. 2021; Hsu et al. 2022; Bouvier et al. 2022). It remains unknown why some sources show rich emission of gas-phase organics and others do not. It may be a true chemical effect, with some sources having low ice-phase COM reservoirs due to their environmental/evolutionary conditions. Another possibility is that COMs are only efficiently sublimated into the gas phase in a subset of sources. Disk shadowing can effectively lower the temperature in the envelope, leading to inefficient desorption and thus low abundance of gaseous COMs, hence nondetection (Nazari et al. 2022). Moreover, high dust optical depth could suppress the COM emission at submillimeter wavelengths (De Simone et al. 2020; Nazari et al. 2022). Disentangling these scenarios requires an understanding of COM abundances in the ice phase. Therefore, mid-infrared spectroscopy of organic ice features offers an avenue to understand the origin and nature of complex molecule formation in protostars.

Outflows are ubiquitously associated with protostellar cores. The clearance of an outflow cavity and the accretion activity that is tightly related to outflows regulates the thermal structure of the envelope as well as the photochemistry along the cavity wall, thus affecting the abundance of COMs in both gas and ice phases (e.g., Visser et al. 2012; Drozdovskaya et al. 2014, 2015). At mid-infrared wavelengths, rotationally excited H₂ lines and ionic forbidden lines trace the shocked gas and jets in outflow cavities (e.g., Lahuis et al. 2010). Furthermore, rovibrational CO lines and water vapor emission at $\sim 4\text{--}6\ \mu\text{m}$ highlight the shocked gas at the base of outflows and/or at the disk surface, constraining the physical conditions of outflows and disks (e.g., Herczeg et al. 2011; Salyk et al. 2022).

The COMs ORigin Investigated by the Next-generation Observatory in Space (CORINOS) program measures the ice composition of four isolated Class 0 protostars with JWST (program 2151, PI: Y.-L. Yang). The program aims to determine the abundances of ice species with radiative transfer and chemical modeling to constrain the formation and evolution of COMs. The full sample consists of two protostars whose gas-phase spectra are known to exhibit rich COM features, B335 and L483, and two protostars with little emission of gas-phase COMs, IRAS 15398–3359 and Ser-emb 7 (Sakai et al. 2009; Imai et al. 2016; Oya et al. 2017; Bergner et al. 2019a; Jacobsen et al. 2019). Each pair represents low-luminosity ($\sim 1\ L_{\odot}$) and high-luminosity ($\sim 10\ L_{\odot}$) protostars. This work presents initial results from the first observation of IRAS 15398–3359.

In this Letter, we present JWST/Mid-Infrared Instrument (MIRI) observations of IRAS 15398–3359, highlighting several new mid-infrared ice features, likely associated with COMs, as well as emission lines and outflows detected in both spectroscopy and imaging. In Section 2, we describe our JWST/MIRI observing program and data reduction. In Section 3, we show the extracted 1D Medium Resolution Spectroscopy (MRS) spectra and identify absorption features in the spectra along with possible contributing ice species. Section 4 presents the detection of warm water vapor and CO emission, which may originate in a young protoplanetary disk. Section 5 shows the southwestern outflow of IRAS 15398–3359 in MIRI imaging and presents detected emission lines, most of which trace the outflows and jets. Finally, in Section 6, we highlight the findings with this first analysis of JWST/MIRI spectra of a Class 0 protostar.

1.1. IRAS 15398–3359

IRAS 15398–3359 (also known as B228) is a Class 0 protostar located in the Lupus I Molecular Cloud (Heyer & Graham 1989; Chapman et al. 2007) at a distance of $154.9^{+3.2}_{-3.4}$ pc (Galli et al. 2020). It has a bolometric luminosity (L_{bol}) of $1.5\ L_{\odot}$ and a bolometric temperature (T_{bol}) of 68 ± 27 K (Yang et al. 2018; Vazzano et al. 2021). IRAS 15398–3359 has drawn astrochemical interest because of its abundant warm carbon-chain molecules (CCMs), which suggests an active warm carbon-chain chemistry (WCCC; Sakai et al. 2009) and chemical signatures of episodic accretion (e.g., Jørgensen et al. 2013). In the WCCC scenario, abundant CH₄ ice, which may form in the prestellar stage, is sublimated as the temperature increases due to accretion heating, leading to an elevated abundance of carbon carriers available for the formation of CCMs (Aikawa et al. 2008; Sakai et al. 2008). High UV illumination at the prestellar stage may explain abundant carbon-chain molecules in protostars (Spezzano et al. 2016). On the other hand, only a few emission lines of complex organic molecules (COMs) have been detected despite its rich CCMs (Y. Okoda et al. 2022, in preparation). The location of the envelope water snow line inferred from HCO⁺, as well as by detection of HDO, is larger than the current luminosity of IRAS 15398–3359 (Jørgensen et al. 2013; Bjerkeli et al. 2016b), suggesting a higher luminosity in the last 100–1000 yr, perhaps due to an accretion burst. Moreover, the ice features of IRAS 15398–3359 were studied in the Spitzer Cores to Disks (“c2d”) survey, where common species, such as H₂O, CO₂, CH₄, and CH₃OH, were identified (Boogert et al. 2008; Öberg et al. 2008; Pontoppidan et al. 2008; Bottinelli et al. 2010).

IRAS 15398–3359 is associated with a compact disk, although poorly constrained by observations. Yen et al. (2017) estimated a centrifugal radius ($R_c = \frac{j^2}{GM_*}$, where j is the specific angular momentum) of 20^{+50}_{-20} au by fitting the C¹⁸O emission. With a similar method, Okoda et al. (2018) found the centrifugal barrier ($R_{\text{cb}} = \frac{j^2}{2GM_*}$) at 40 au can explain the kinematics of the SO emission, which corresponds to a centrifugal radius of 80 au. The estimated disk radii from both studies are consistent with considerable uncertainty due to the unresolved Keplerian rotation. They also estimated a very low protostellar mass of only $\leq 0.01^{+0.02}_{-0}\ M_{\odot}$ and $0.007^{+0.004}_{-0.003}\ M_{\odot}$ by Yen et al. (2017) and Okoda et al. (2018), respectively.

The bipolar outflow of IRAS 15398–3359 has a young dynamical age of ~ 1000 yr, as measured from the CO outflow

(Yildız et al. 2015; Bjerkeli et al. 2016a). The outflow consists of a wide-angle wind-driven outflow and jet-driven bow shocks (Bjerkeli et al. 2016a; Yen et al. 2017). Okoda et al. (2020) show compact emission of H_2CO in the outflow identified with a principal component analysis, suggesting a shock-induced origin. Vazzano et al. (2021) further showed evidence of a precessing episodic jet-driven outflow with four ejections separated by 50–80 yr. Recently, Okoda et al. (2021) found an arc-like structure perpendicular to the known outflow, which they interpreted as shocked gas due to a previously launched secondary outflow.

2. Observations

The protostar IRAS 15398–3359 was observed with MIRI (Rieke et al. 2015; Wright et al. 2015) on board JWST on 2022 July 20, as part of program 2151 (PI: Y.-L. Yang). The observations used the MRS mode, which is equipped with four integral field units (IFUs) that observed the target simultaneously using dichroics. These IFUs are often referred as “channels,” where channels 1, 2, 3, and 4 cover 4.9–7.65, 7.51–11.71, 11.55–18.02, and 17.71–28.1 μm , respectively. Each channel is covered by the same three grating settings, which are also called “subbands.” Thus, an exposure with only one grating setting results in four discontinuous spectra. A full 4.9–28 μm coverage requires observations with three grating settings, resulting in 12 spectral segments. The spectroscopic data were taken in SLOWR1 readout mode with a standard four-point dither pattern.

IRAS 15398–3359 was observed with a pointing center on ($15^{\text{h}}43^{\text{m}}02^{\text{s}}24$, $-34^{\circ}09'06''7$) based on the submillimeter continuum peak from Oya et al. (2014) along with a dedicated background pointing centered on ($15^{\text{h}}43^{\text{m}}07^{\text{s}}9$, $-34^{\circ}09'01''$). Recent Atacama Large Millimeter/submillimeter Array (ALMA) observations suggest a submillimeter continuum peak at ($15^{\text{h}}43^{\text{m}}02^{\text{s}}2307$, $-34^{\circ}09'06''99$) using the ALMA Band 6 observations taken on 2022 May 16 (2021.1.00357.S; PI: S. Notsu). The integration time is 1433.4 s for the SHORT(A) and LONG(C) subbands and 3631.3 s for the MEDIUM(B) subband. The MEDIUM(B) subband covers the 8.67–10.15 μm range where the intensity is the lowest due to strong absorption of silicates. Thus, we intentionally integrated longer with the MEDIUM(B) setting to achieve a sufficient signal-to-noise ratio (S/N) to characterize the ice features around the silicate feature.

The data were processed from the Stage 1 data files (uncal) using v1.7.2 of the JWST pipeline and CRDS context (jwst_0977.pmap) from <https://jwst-crds-pub.stsci.edu/>. The dedicated background exposures were subtracted on the exposure level during Stage 2 of the pipeline. The Stage 3 process includes `OutlierDetectionStep`, `Residual-FringeStep`, and `CubeBuildStep`. The `Residual-FringeStep` task is included to correct for residual fringes that are not fully corrected by the application of a fringe flat, particularly in extracted point-source spectra. The fringe is suppressed in most subbands except for noticeable residuals in `ch3-long` around 10–12 μm . The wavelength calibration is generally accurate to within ~ 1 spectral resolution element ($\sim 100 \text{ km s}^{-1}$; Rigby et al. 2022).

The protostar appears pointlike in the MRS spectral cube. Thus, we extracted a 1D spectrum with an aperture (R_{ap}) defined by the diffraction-limited beam size ($1.22\lambda/D$) so that the aperture increases with wavelength. The aperture centers at

the ALMA continuum peak ($15^{\text{h}}43^{\text{m}}02^{\text{s}}2307$, $-34^{\circ}09'06''99$). We tested the spectral extraction with additional local background subtraction derived from an annulus outside the aperture; however, the resulting spectra appear to have more noise possibly because the extended outflow cavity complicates the determination of the true background. Thus, we performed no additional background subtraction on the reduced spectral cubes. Despite its pointlike appearance, the source emission extends beyond the size of the diffraction-limited beam. A 1D spectrum extracted with a small aperture results in inconsistent flux between several subbands due to the flux extended beyond the aperture. Appendix A shows a detailed analysis of the extracted spectra with different apertures. We find that a four-beam aperture provides a good balance between the flux agreement between subbands and noise. All spectra shown in this study are extracted with a four-beam aperture, $4 \times 1.22\lambda/D$, unless otherwise specified. We further matched the flux between channels by the ratio of median fluxes in the overlapping wavelengths by applying scale factors of order $\lesssim 16\%$, starting from the shortest wavelength. The scaled spectrum differs from the original spectrum by at most 16%.

To estimate the rms in the extracted 1D spectrum, we subtracted a Gaussian-smoothed baseline and calculated the rms in the residual with respect to the smoothed baseline, which has a median of 0.8% with a 1σ range from 0.4% to 1.3%. The Gaussian width is chosen as 20 wavelength channels to approximate the baseline without noise and avoid smoothing out broad absorption features. The rms may be underestimated between 10 and 12 μm , where the fringe residuals are not fully suppressed.

Simultaneous MIRI imaging was enabled along with the primary spectroscopic observations for astrometric registration. The simultaneous field is pointed off the MRS target, but the background observation happened to be arranged such that it covered the southwestern outflow lobe of IRAS 15398–3359. The imaging fields were observed with FASTR1 readout pattern, in the F560W, F770W, and F1000W filters, with filter widths of 1.2, 2.2, and 2.0 μm , respectively. The point-spread function (PSF) FWHM in these bands was measured to $0''.22$, $0''.25$, and $0''.32$, respectively. The total exposure time was 1433.4, 1433.4, and 3631.3 s, the same as their spectroscopic counterparts. The Stage 3 products were generated by the standard pipeline obtained from the Barbara A. Mikulski Archive for Space Telescopes (MAST); the data were calibrated with `jwst_0932.pmap` from <https://jwst-crds.stsci.edu/> without further reprocessing. The rms noise estimated from the standard deviation in an empty sky region is 2.3, 7.6, and 18.4 MJy sr^{-1} , respectively.

3. Ice Bands in the Point-source Spectrum

The extracted MIRI MRS spectrum shows strongly increasing flux density with wavelength along with several absorption features, which is typical for embedded protostars (Figure 1, top). All of the identified absorption features are due to ices and silicates. We estimate the large-scale continuum by fitting a fourth-order polynomial using the 5.05–5.15 μm , 5.3–5.4 μm , and 5.52–5.62 μm ranges of the MRS spectrum and the 35–38 μm range of the scaled Spitzer/InfraRed Spectrograph (IRS) spectrum (see Figure B1, right). Ideally the spectrum at the longest wavelengths, which is less affected by silicate and H_2O absorption, would be included for the continuum fitting. However, the long-wavelength end ($>27.5 \mu\text{m}$) of the MRS

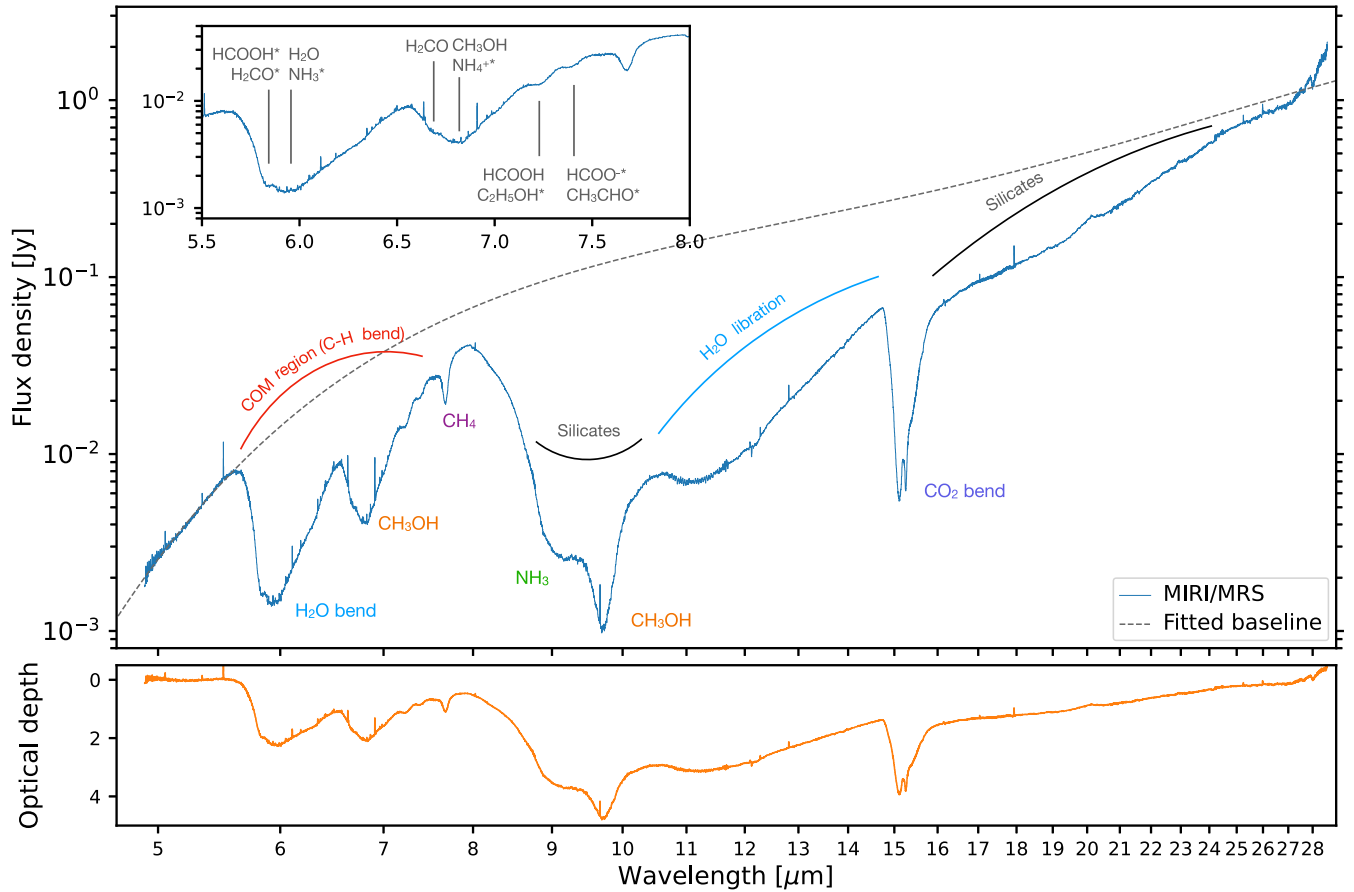


Figure 1. Top: extracted MIRI MRS spectrum of the IRAS 15398–3359 point source, with major solid-state features indicated. The wavelength axis is in logarithmic scale. The dashed line illustrates the fitted continuum. Top (inset): detail of the 5.5–8 μm region from the same spectrum with secure and possible identifications labeled (see Table 1). Bottom: the optical depth spectrum derived using the continuum shown in the top panel.

spectrum has higher noise and a steeper slope compared to the spectrum at 16–27 μm ; thus, we consider the $>27.5 \mu\text{m}$ spectrum as less reliably calibrated compared to the rest of the spectrum due to the rapid drop in MRS sensitivity at its longest wavelengths. Including the Spitzer/IRS spectrum allows us to perform the continuum fitting at longer wavelengths ($>30 \mu\text{m}$). The fitted continuum is consistent with the long-wavelength end of the MIRI MRS spectrum. Nonetheless, this fit has substantial systematic uncertainty depending on various factors, such as the choice of assumed absorption-free ranges and the functional form of the continuum. The qualitative analysis presented here serves to identify potential carriers of the ice bands, rather than to derive precise ice abundances.

Figure 1 (bottom) shows the optical depth spectrum, derived as $\tau = -\ln(F/C)$, where F is the flux density and C is the fitted continuum. We clearly detect the silicate band centered at 10 μm , as well as the bending and libration modes of H_2O ice at 6 and 11–13 μm , respectively. We also securely detect CH_3OH via the strong band at 9.7 μm , supported by substructure at 6.8 μm , CH_4 at 7.7 μm , and CO_2 via its bending mode at 15.2 μm . In addition, we highlight notable absorption features due to minor species that still have ambiguous identifications. The features and qualitative description of their shape are listed in Table 1, where tentative identifications are marked with asterisks. In the following paragraphs, we discuss individual features.

Table 1
Notable Ice Features

Wavelength (μm)	Type	Identification
5.83	single	HCOOH^a , H_2CO^a
6	multiple	H_2O , NH_3^a
6.7	single	H_2CO
6.8	multiple	CH_3OH , $\text{NH}_4^+^a$
7.24	single	HCOOH , $\text{C}_2\text{H}_5\text{OH}^a$
7.41	single	HCOO^-^a , CH_3CHO^a
7.7	single	CH_4 , SO_2^a , $\text{C}_2\text{H}_5\text{OH}^a$
9	single	NH_3 , CH_3OH^a , $\text{C}_2\text{H}_5\text{OH}^a$
9.7	single	CH_3OH
11	single/broad	H_2O , $\text{C}_2\text{H}_5\text{OH}^a$, CH_3CHO^a , HCOOCH_3^a
15.2	multiple	CO_2

Note.

^a Potential/ambiguous identification.

3.1. Individual Features

3.1.1. 5.83 μm Feature: HCOOH^* and H_2CO^*

This feature is likely due to the C=O stretching mode of HCOOH (Maréchal 1987; Bisschop et al. 2007) and/or H_2CO (Schutte et al. 1993). The feature is seen in the MIRI spectrum

* Potential/ambiguous identification.

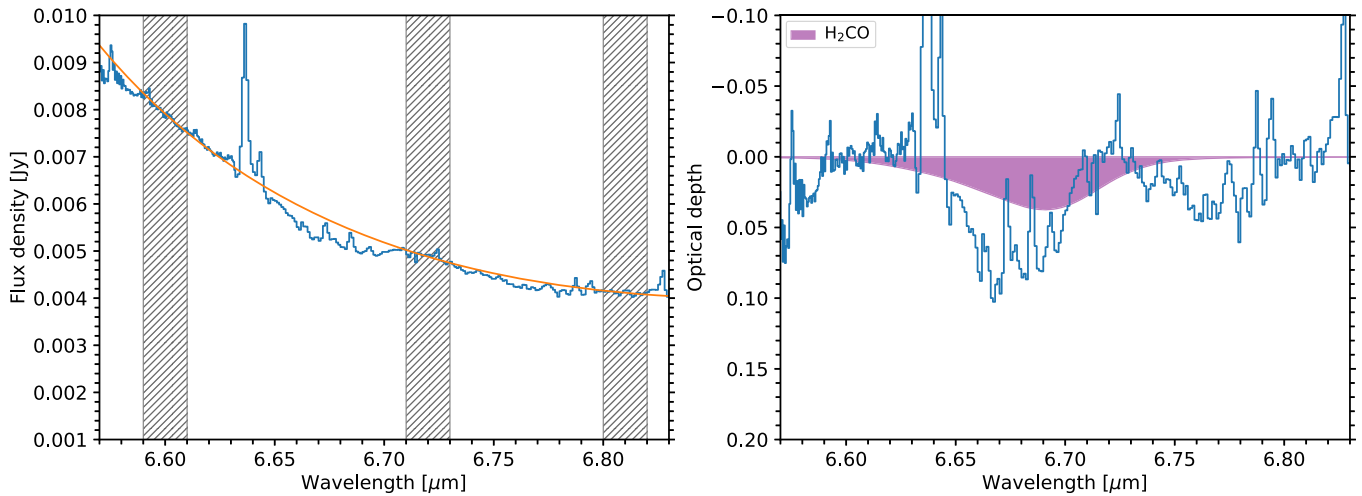


Figure 2. Left: the MIRI MRS spectrum of IRAS 15398–3359 along with a second-order polynomial baseline fitted at 6.59–6.61 μm and 6.79–6.81 μm (gray hatched regions). Right: the optical depth spectra of the shallow absorption at 6.68–6.72 μm . The purple shaded region shows the scaled laboratory absorbance spectrum from Gerakines et al. (1996). The narrow emission features are predominantly due to warm gas-phase water (Section 4).

as a blue shoulder on the broad ($\sim 0.5 \mu\text{m}$) feature of the H_2O bending mode in the 5.8–6.3 μm region (Schutte et al. 1996). Boogert et al. (2008) measured the abundance of HCOOH as 1.9% relative to H_2O using the 7.25 μm feature of HCOOH , which we also detect (Section 3.1.5). Even if the identification of HCOOH is independently confirmed, both species could contribute to this C=O stretching mode at 5.8 μm . In fact, Boogert et al. (2008) showed that H_2CO can contribute no more than 10%–35% of this feature based on the nondetection of its absorption features at 3.34, 3.47, and 3.54 μm in L -band spectra of other sources.

3.1.2. 6 μm Feature: H_2O and NH_3^*

The H_2O bending mode peaks at 6 μm , dominating this feature (e.g., Keane et al. 2001). The N–H deformation mode of NH_3 at 6.16 μm , whose umbrella mode at 9 μm is detected (Section 3.1.8), also contributes to this broad feature (Boogert et al. 2008). While the 6 μm feature is detected in all low-mass protostars, the absorption from H_2O and NH_3 often underestimates the depth of this feature, suggesting additional contributions from unidentified species.

3.1.3. 6.7 μm Feature: H_2CO

We detect a shallow inflection on the blue side of the 6.8 μm band (Section 3.1.4). Schutte et al. (1993) reported that the C–H bending mode of H_2CO occurs at 6.68 μm . In the c2d survey, Boogert et al. (2008) put an upper limit of 15% contribution from this bending mode to the absorption feature centered on 6.85 μm . In our MIRI spectrum, the optical depth of this feature is ~ 0.05 with a local baseline fitting (Figure 2) and the overall optical depth of the entire 6.8 μm band is ~ 1.5 , consistent with the suggested upper limit.

3.1.4. 6.8 μm Feature: CH_3OH and NH_4^*

This feature is ubiquitous in icy sight lines toward protostars and in the dense interstellar medium, and IRAS 15398–3359 is no exception. Its position and shape is broadly consistent with

the C–H bending mode of CH_3OH (Boogert et al. 2008). Schutte & Khanna (2003) proposed that NH_4^+ could be a significant contributor; however, the identification of NH_4^+ , based on the 6.8 μm band alone remains debated, while CH_3OH can be confirmed given the observation of the corresponding C–O stretching mode at 9.75 μm in IRAS 15398–3359 (Section 3.1.9).

3.1.5. 7.24 μm Feature: HCOOH and $\text{C}_2\text{H}_5\text{OH}^*$

This feature was tentatively detected in IRAS 15398–3359 among a few other low-mass protostars, as well as high-mass protostars (Schutte et al. 1999; Boogert et al. 2008), but the low S/N of the optical depth spectra prohibited a robust carrier identification. We clearly detect the band at a high level of significance (Figure 3). This feature could be associated with the CH_3 symmetric deformation mode of $\text{C}_2\text{H}_5\text{OH}$ (Öberg et al. 2011; Terwisscha van Scheltinga et al. 2018) and/or the C–H/O–H deformation mode of HCOOH (Schutte et al. 1999; Bisschop et al. 2007). The band strength of the HCOOH 7.24 μm feature is ~ 25 times weaker than that of its 5.83 μm feature (Bisschop et al. 2007). Conversely, we estimate $\tau_{5.8 \mu\text{m}}/\tau_{7.24 \mu\text{m}} \sim 1.4$. Despite considerable uncertainty in the fitted baseline and the H_2O absorption at 5.8 μm , other species, such as $\text{C}_2\text{H}_5\text{OH}$, may also contribute to the observed feature (Table C2).

3.1.6. 7.41 μm Feature: HCOO^* and CH_3CHO^*

This feature was tentatively seen in Spitzer/IRS spectra, but is clearly detected in the MIRI spectrum at high confidence. This feature may be due to the C=O stretching mode of HCOO^- (Schutte et al. 1999) and/or the CH_3 symmetric deformation with the C–H wagging mode of CH_3CHO (Öberg et al. 2011; Terwisscha van Scheltinga et al. 2018). HCOO^- has another C=O stretching mode at 6.33 μm , where the observed spectrum has a slight bending feature at $\sim 6.31 \mu\text{m}$. CH_3CHO , on the other hand, has a feature at 7.427 μm , located at a slightly longer wavelength than the observed feature.

* Potential/ambiguous identification.

* Potential/ambiguous identification.

* Potential/ambiguous identification.

* Potential/ambiguous identification.

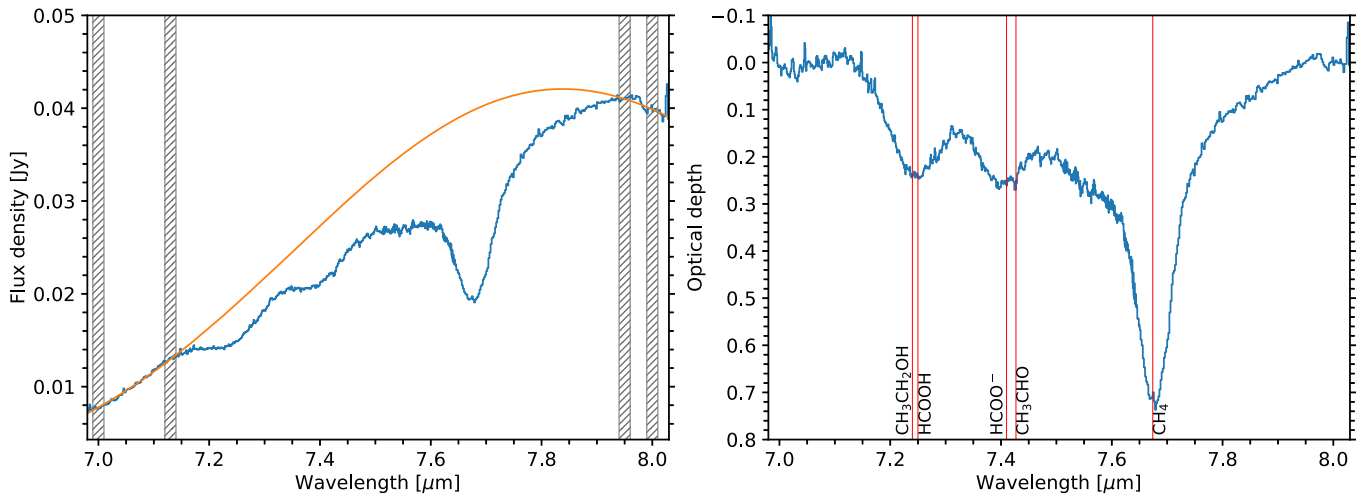


Figure 3. Ice features in the spectra from 7 to 8 μm . Left: the MRS spectra and the fitted continuum. The continuum is fitted locally with a third-order polynomial anchored at 6.99–7.01 μm , 7.12–7.14 μm , 7.94–7.96 μm , and 7.99–8.01 μm (gray hatched regions). Right: the optical depth spectra labeled with potential carriers.

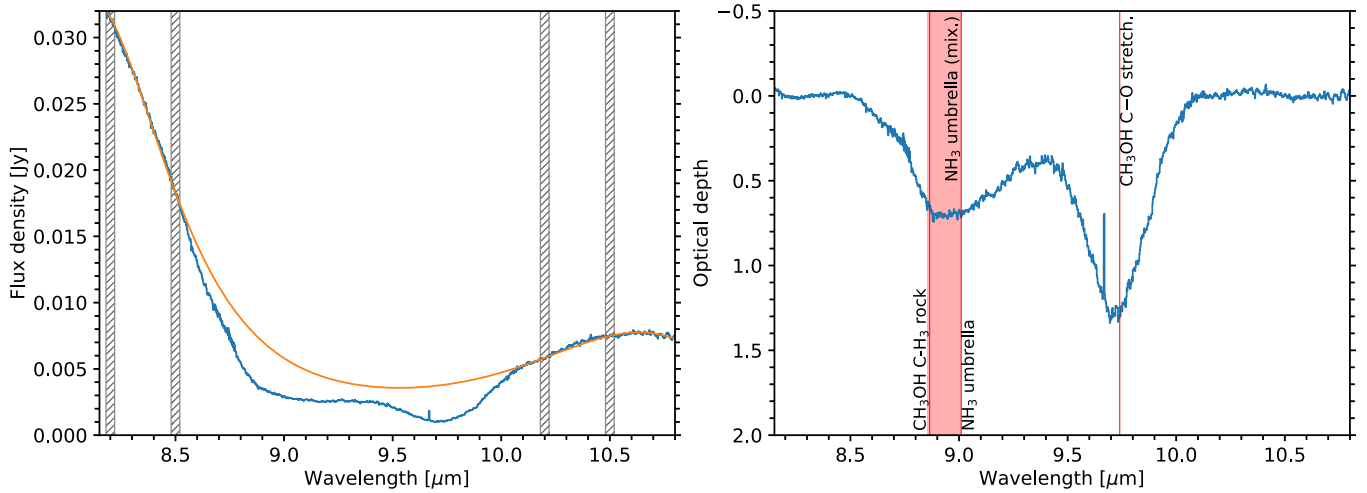


Figure 4. Ice features in the 8–11 μm region of the spectrum. Left: the MRS spectrum and the continuum fit. The continuum is fitted locally with a fourth-order polynomial using 8.18–8.22 μm , 8.48–8.52 μm , 10.18–10.22 μm , and 10.48–10.52 μm as anchor points (gray hatched regions). Right: the optical depth spectrum labeled with potential carriers. The red shaded region highlights the range of the NH₃ umbrella mode in various ice mixtures investigated in Bottinelli et al. (2010).

However, the peak position could move to 7.408 μm depending on the ice mixture of CH₃CHO (Terwisscha van Scheltinga et al. 2018). Thus, both species are potential contributors to this feature.

3.1.7. 7.7 μm Feature: CH₄

This is a common feature attributed to the CH₄ deformation mode (Boogert et al. 2008). The optical depth of CH₄ is ~ 0.6 , while Öberg et al. (2008) measured a peak optical depth of 0.22 ± 0.03 using Spitzer data. The lower optical depth may be due to the much lower spectral resolving power ($R \sim 100$; $\Delta\lambda \sim 0.08 \mu\text{m}$) that underresolves the narrow absorption feature (FWHM $\sim 0.07 \mu\text{m}$). The higher spatial resolution in the MRS data may also result in a higher CH₄ optical depth, which varies spatially. SO₂ ice has a feature at 7.63 μm with a width of $\sim 0.15 \mu\text{m}$ (Boogert et al. 1997). We cannot distinctively identify the contribution of SO₂ because of potential contribution from organic species, such as C₂H₅OH (Table C2).

3.1.8. 9 μm Feature: NH₃

Both the CH₃ rocking mode of CH₃OH at 8.87 μm and the umbrella mode of NH₃ at 9.01 μm are likely to contribute to this feature (Figure 4). The former feature is narrower (FWHM = 0.24 μm) than the latter (FWHM = 0.58 μm). Bottinelli et al. (2010) showed that the peak position of the NH₃ umbrella mode could shift toward shorter wavelengths when mixed with H₂O and/or CH₃OH. C₂H₅OH has its CH₃ rocking mode at 9.17 μm and C–O stretching mode at 9.51 μm . However, both features are very narrow (FWHM ~ 0.1 –0.2 μm), and are not clearly visible in the MIRI spectra.

3.1.9. 9.7 μm Feature: CH₃OH

This feature is commonly attributed to the C–O stretching mode of CH₃OH at 9.74 μm . While the peak and width of the observed feature matches the expected CH₃OH absorption feature, there is slightly more absorption at the shorter-wavelength side of the feature, hinting at contribution from other species, such as NH₃ and C₂H₅OH (Section 3.2). A

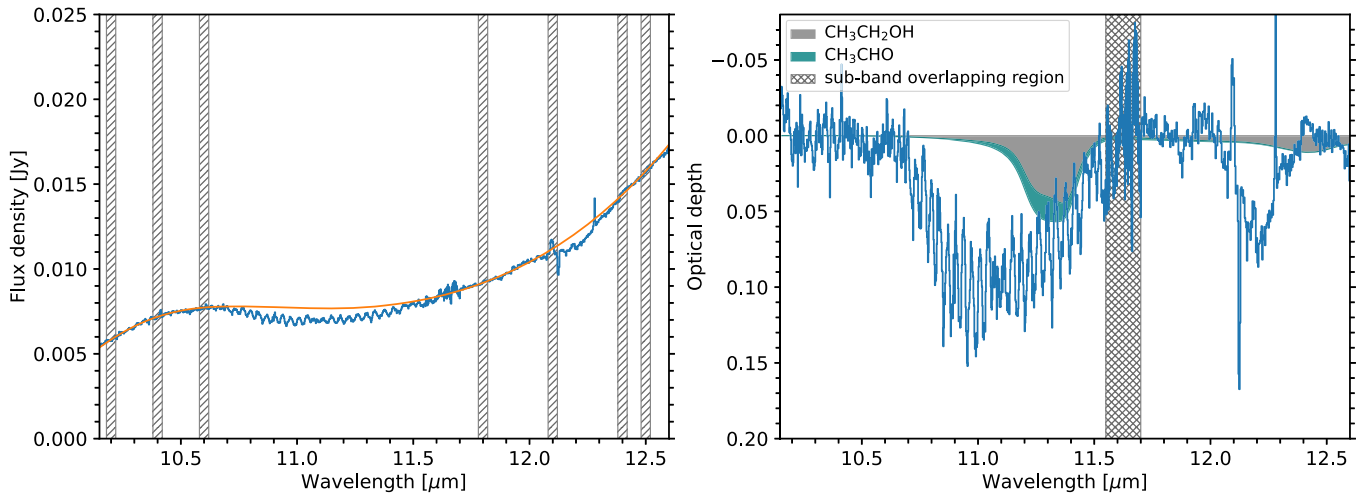


Figure 5. Ice features in the 11–12 μm region of the spectrum. Left: the MRS spectrum and the continuum fit. The continuum is fitted locally with a fifth-order polynomial using $\pm 0.01 \mu\text{m}$ regions around 10.18–10.22 μm , 10.38–10.42 μm , 10.58–10.62 μm , 11.78–11.82 μm , 12.18–12.22 μm , 12.38–12.42 μm , and 12.48–12.52 μm as anchor points (gray hatched regions). Right: the optical depth spectra compared to laboratory spectra of $\text{C}_2\text{H}_5\text{OH}$, CH_3CHO , and HCOOCH_3 . The crosshatched region highlights the overlapping range of two subbands, which has a less stable baseline.

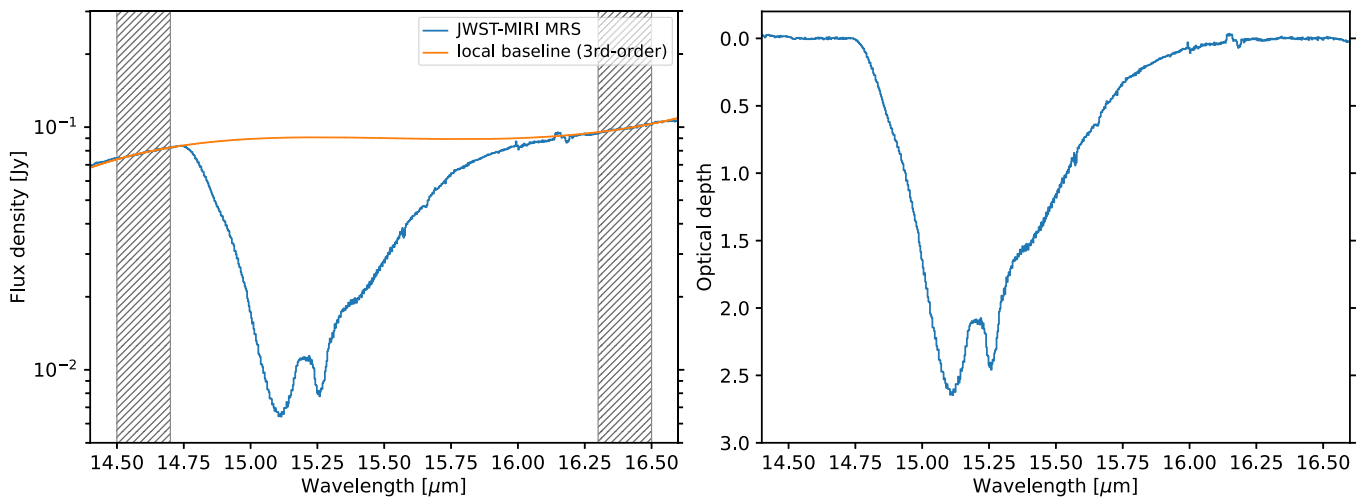


Figure 6. Spectra of the CO_2 ice feature at 15.2 μm . The MIRI spectra zoomed to the CO_2 ice features are shown in the left panel. A local baseline (orange) is fitted with a third-order polynomial using the spectra in 14.5–14.7 μm and 16.3–16.5 μm . The derived optical depth spectra are shown in the right panel.

model of the silicate band, taking into account grain composition and size distribution, is required to accurately extract the profiles of the ice bands in this region, which is beyond the scope of this overview Letter.

3.1.10. 11 μm Feature: H_2O Libration

This feature is very broad, spanning 10–13 μm , consistent with the well-known H_2O libration mode, which can extend to 30 μm . Bregman et al. (2000) reported a narrower, weak absorption feature at 11.2 μm , interpreted as polycyclic aromatic hydrocarbon (PAH) mixtures. Crystalline silicates, especially forsterite, also have absorption features around $\sim 11 \mu\text{m}$ (Kessler-Silacci et al. 2005; Wright et al. 2016; Do-Duy et al. 2020). Finally, Terwisscha van Scheltinga et al. (2021) showed that $\text{C}_2\text{H}_5\text{OH}$, CH_3CHO , and HCOOCH_3 could produce absorption at similar wavelengths. Figure 5 shows the presence of an unambiguous 11.2 μm feature in the MIRI spectrum. Determining the carrier of this feature would require additional modeling.

3.1.11. 15.2 μm CO_2

This ubiquitous feature is due to the bending mode of CO_2 (Figure 6). The double peaks are a distinctive signature of crystalline, usually relatively pure, CO_2 ice (Ehrenfreund et al. 1997). There are two broader features at 15.1 and 15.3 μm , corresponding to the apolar CO_2 : CO mixture and the polar CO_2 : H_2O mixture, respectively. The shoulder extending toward longer wavelengths is due to CO_2 mixed with CH_3OH . Pontoppidan et al. (2008) detected the double-peaked CO_2 with Spitzer in the same source; however, the strength of those peaks was weaker than the MRS spectra indicate. The significantly improved spectral resolution may lead to stronger peaks, but constraining the origin of such change, such as a temporal variation, requires further modeling.

Pure CO_2 ice only form in regions with elevated temperature, at ~ 50 –80 K via the thermal annealing process (Gerakines et al. 1999; Escribano et al. 2013; He et al. 2018) or at ~ 20 –30 K via the distillation of a CO_2 : CO mixture (Pontoppidan et al. 2008). Kim et al. (2011) suggest that detection of pure CO_2 in low-luminosity protostars could be

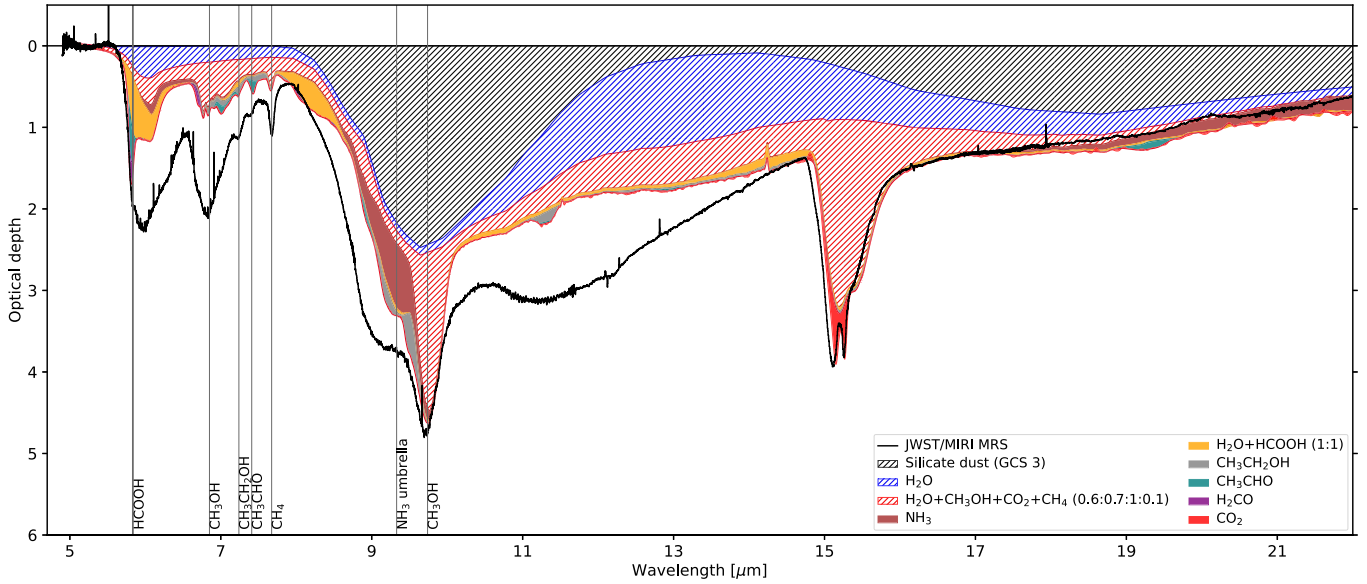


Figure 7. Optical depth spectra compared with a composite spectra of several ice species measured from experiments. The details of the laboratory data are discussed in Appendix C. The “CO₂” spectra (red) are from pure CO₂.

indicative of previous episodic accretion. In fact, Jørgensen et al. (2013) found a ring-like (inner radius of 150–200 au) structure of H¹³CO⁺ emission with ALMA, suggesting that water vapor is present on small scales destroying H¹³CO⁺ (Phillips et al. 1992). The origin of this water vapor could be an accretion burst that occurred 100–1000 yr ago, increasing the luminosity by a factor of 100, making such an interpretation for the CO₂ double peak a viable explanation. In the distillation scenario, both a warm disk and the inner envelope can provide suitable environments; however, a well-defined Keplerian disk has not yet been detected in IRAS 15398–3359.

3.2. Composite Ice Spectra

The unprecedented S/N combined with the subarcsecond spatial resolution allows a multicomponent ice spectral comparison with laboratory data across the entire range of MIRI coverage (4.9–28 μm). As discussed in Section 3.1, many absorption features are likely to have several contributing ice species, and only the strongest features could be robustly identified by previous studies. The highly sensitive MIRI MRS spectrum enables a comprehensive approach to compare composite optical depth spectra including multiple ice species. Figure 7 shows a simple composite synthetic spectrum of several ice species discussed in Section 3.1. We also include the spectrum of GCS 3, representing the silicate dust (Kemper et al. 2004). The optical depth spectrum of each ice species and mixture is scaled to match the observations. While we do not aim to fit the observed optical depth spectra, we can already see wavelength regions where the laboratory ice spectra reproduce the observations in this toy model, such as ~10 μm and ~15 μm. This simple model underestimates the absorption at 5–9 μm and 11–12 μm regions, calling for detailed ice modeling in future studies. This experiment demonstrates the vast potential of JWST/MIRI spectroscopy for studies of interstellar ices.

4. Warm Water Vapor and CO Gas as a Signpost of the Embedded Disk

JWST provides spatial resolution similar to that achieved by ALMA, allowing us to search for signatures of the embedded disk suggested by ALMA observations (Yen et al. 2017; Okoda et al. 2018). Warm water and CO gas at the *M* band (4.7–5 μm) are a common tracer of the inner disk in Class I and II sources (Pontoppidan et al. 2003; Banzatti et al. 2022), but they have rarely been detected in Class 0 sources, like IRAS 15398–3359. In Figure 8, we compare the baseline-subtracted 4.9–7.3 μm region of the IRAS 15398–3359 spectrum with a simple slab model of warm water vapor (~200–300 K) and CO fundamental ($\nu = 1 - 0$ and $2 - 1$) rovibrational lines at a higher temperature (Salyk et al. 2011; Salyk 2020). The synthetic spectra are multiplied with the continuum to account for variable extinction on these emission lines, which fit the data better. The molecular data are taken from HITRAN (Gordon et al. 2022). The water lines appear prominently from 5.8–7.3 μm, while the (P-branch; $\Delta J = -1$) CO appears at the shortest MIRI wavelengths (4.9–5.3 μm). Although these models are not adapted to this source, it is clear from inspection that the region contains a large number of compact emission lines.

The agreement between model and observation is considerable. We can state with confidence that the majority of this emission comes from a compact region of the source, and is attributable to warm water vapor, which is likely excited in the previously undetected embedded disk region, within the inner 0.2, and/or the shocked gas in the inner envelope. The specific model fits and constraints on the spatial extent of the emission are left to a future work.

5. Outflows and Jets

5.1. MIRI Imaging

The parallel imaging of our background pointing serendipitously covered the blueshifted outflow of IRAS 15398–3359.

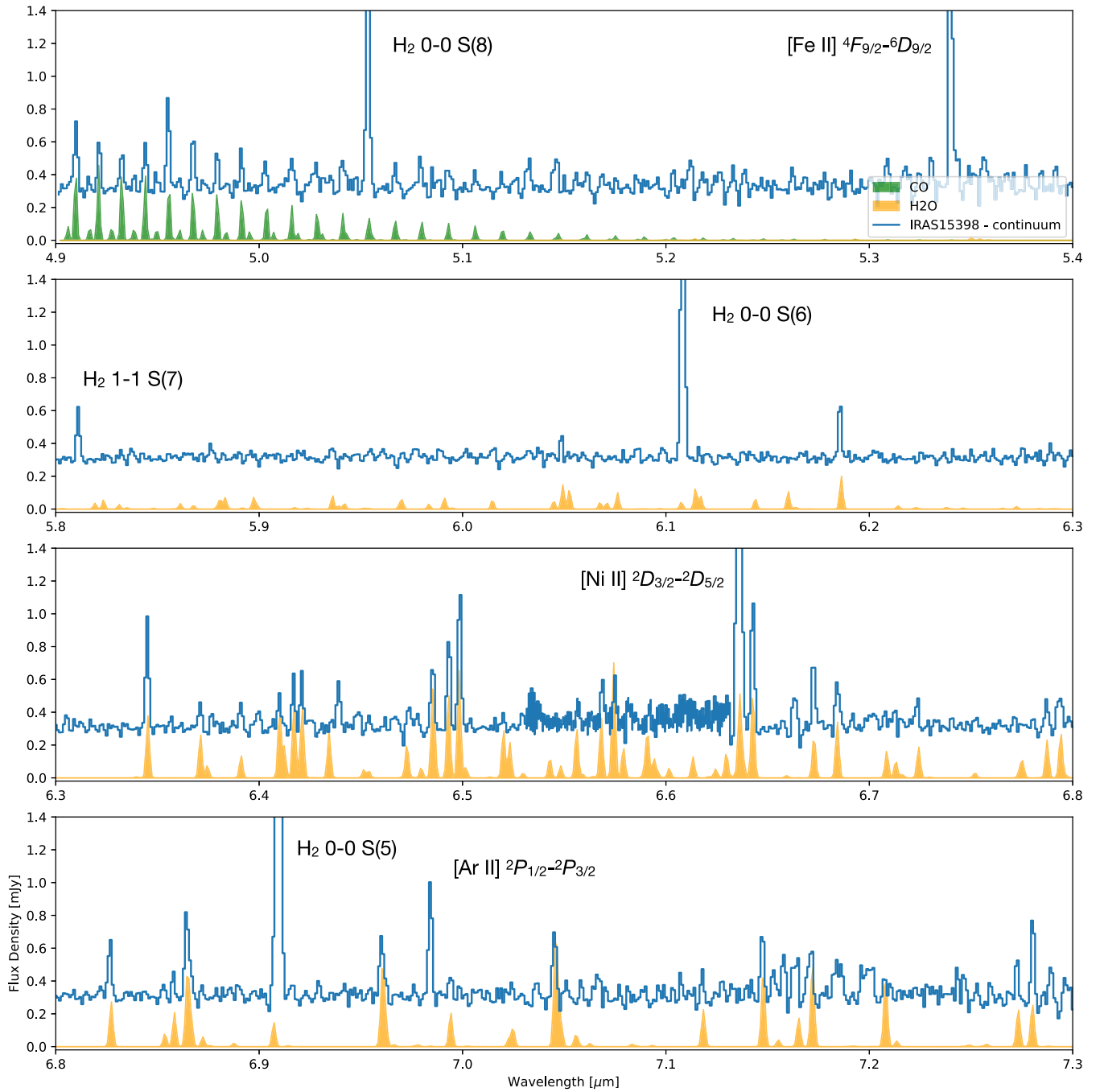


Figure 8. Continuum-subtracted spectra showing emission from the CO fundamental P-branch and the H₂O bending mode centered on 6 μ m. The data, which are shown with an offset of 0.3 mJy, are modeled by a simple slab model for line identification (Salyk et al. 2011; Salyk 2020). Emission lines other than H₂O and CO are annotated.

Figure 9 shows the MIRI images of the blueshifted outflows in three filters. The F560W image contains both the continuum and the H₂ S(7) line; the F770W image includes the continuum and the H₂ S(4) line; and the F1100W image consists of the continuum and the H₂ S(3) line. These images unveil exquisite details in the outflow, showing at least four shell-like structures. The outermost shell appears similar to a terminal bow shock. The opening angle of each shell decreases with the distance from the protostar. ALMA observations of outflow tracers, such as CO, H₂CO, and CS, show similar shell-like variations (Bjerkeli et al. 2016a; Okoda et al. 2020, 2021), for which Vazzano et al. (2021) interpret as precessing episodic

outflows driven by a jet. Compared to archival IRAC images taken in 2004 September 3, the terminal shock knot moved by 1''8 along the outflow, which is measured from the centroids of the fitted 2D Gaussian profiles to the blob in the IRAC 3 image and the MIRI F560W image convolved with the IRAC 3 resolution of 1''88 (Figure 9). Considering a length of $\sim 17''$ measured in our MIRI images, the dynamical time of the blueshifted outflow is, thus, ~ 170 yr, suggesting an extremely recent ejection. Vazzano et al. (2021) also identified four ejections separated by 50–80 yr. Interestingly, the mid-infrared outflow has almost the same morphology as the molecular outflow observed in submillimeter.

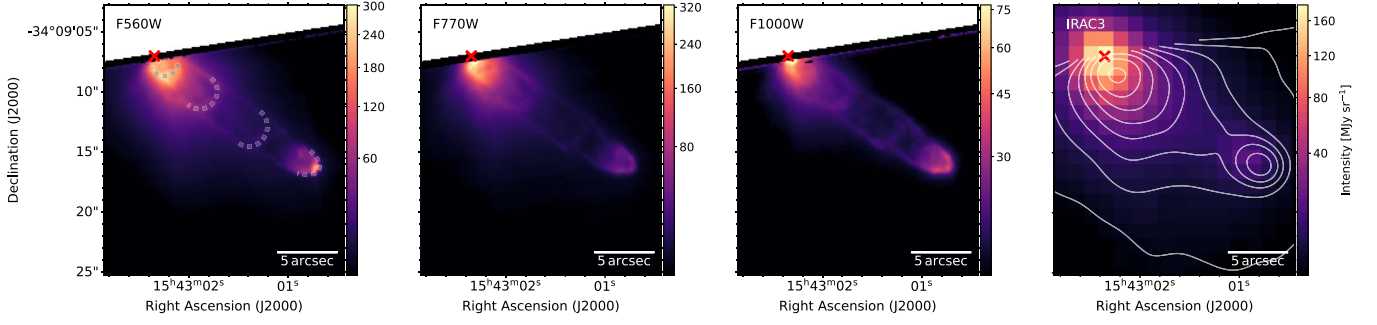


Figure 9. MIRI images with F560W, F770W, and F1000W filters taken in parallel with the background pointing. The identified four shell-like structures are highlights in the panel of the F560W image (left). The image on the right shows the archival Spitzer IRAC 3 image taken on 2004 September 3, where the MIRI F560W image convolved with the IRAC 3 resolution of $1''.88$ is shown in logarithmic contours from 1 to 150 MJy sr^{-1} . The field of view of the MIRI imager leaves a distinct shape at the top left of the images. The red cross labels the submillimeter continuum peak position.

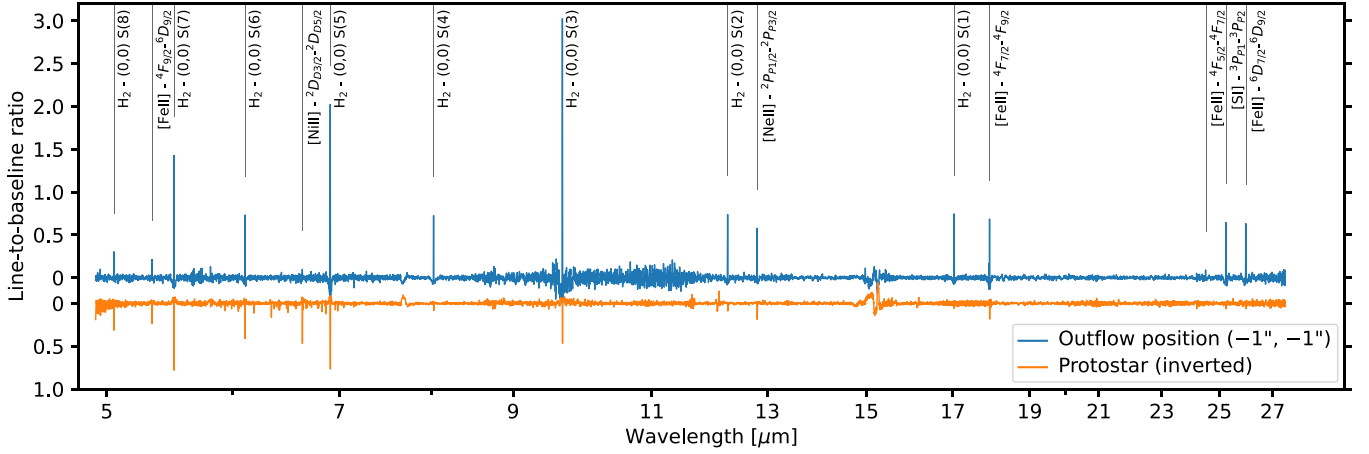


Figure 10. The baseline-divided spectrum extracted on-source (orange) compared with the outflow spectrum extracted at $(-1'', -1'')$ from the submillimeter continuum peak (blue). Both spectra are extracted with a fixed $1''$ aperture. The on-source spectrum is multiplied by -1 for better visual comparison with the outflow spectrum. The weaker emission lines at $5\text{--}7 \mu\text{m}$ in the on-source spectrum are mostly H_2O and CO discussed in Section 4, and the noise in the $\sim 9\text{--}11 \mu\text{m}$ range of both spectra is due to the fringe residual. The continuum is derived by convolving a Gaussian profile with a width of 10 channels. Imperfect continuum subtraction appears around major ice features, such as ~ 7 and $\sim 15 \mu\text{m}$. Identified emission lines are annotated.

5.2. Spectral Line Emission

We also identified several emission lines in the MRS spectra besides the CO and H_2O lines. We extracted a 1D spectrum at $(15^{\text{h}}43^{\text{m}}02^{\text{s}}.15 - 34^{\circ}09'07''.99)$, which is $(-1'', -1'')$ from the submillimeter continuum peak, with an aperture of $1''$ to better probe the emission due to outflow activity (Figure 10). Most lines appear strong in outflows compared to the spectrum toward the protostar, except for the [Ni II] line at $6.636 \mu\text{m}$. Veiling due to scatter light and extinction from the envelope are not considered in this simple extraction, which aims to present a qualitative view of the detected emission lines. As noted in Table 2, most of the strong line emission is identified with either H_2 pure rotational lines or ionized/neutral fine-structure lines from Fe, Ne, or S. Previously with Spitzer IRS spectra, Lahuis et al. (2010) detected H_2 , S(1) and S(4), [Fe II], 17.9 and $26.0 \mu\text{m}$, as well as the [Si II] $35 \mu\text{m}$ in IRAS 15398–3359, the last of which is not covered by MIRI. All of these lines are spatially extended in a bipolar pattern on the NW–SE axis. There is tentative evidence of other weaker emission from the species mentioned in Table 2. We defer a comprehensive analysis of emission lines to a future paper.

Figure 11 shows the continuum-subtracted intensity maps of several representative ionic and molecular lines. The molecular lines, such as H_2 , show a broad opening angle morphology and appear to highlight the walls of the shocked cavity. They also

Table 2
Detected Emission Lines

Wavelength (μm)	Species	Transition
5.053	H_2	0–0 S(8)
5.340	[Fe II]	$^4F_{9/2}\text{--}^6D_{9/2}$
5.511	H_2	0–0 S(7)
5.811	H_2	1–1 S(7)
6.109	H_2	0–0 S(6)
6.636	[Ni II]	$^2D_{3/2}\text{--}^2D_{5/2}$
6.910	H_2	0–0 S(5)
6.985	[Ar II]	$^2P_{1/2}\text{--}^2P_{3/2}$
8.025	H_2	0–0 S(4)
9.665	H_2	0–0 S(3)
12.279	H_2	0–0 S(2)
12.814	[Ne II]	$^2P_{1/2}^0\text{--}^2P_{3/2}^0$
17.035	H_2	0–0 S(1)
17.936	[Fe II]	$^4F_{7/2}\text{--}^4F_{9/2}$
24.519	[Fe II]	$^4F_{5/2}\text{--}^4F_{7/2}$
25.249	[S I]	$^3P_1\text{--}^3P_2$
25.988	[Fe II]	$^6D_{7/2}\text{--}^6D_{9/2}$

show substructures mostly within the southwestern (blue-shifted) outflow cavity. The ionic lines, such as [Fe II] and [Ne II], likely represent hotter regions and are tightly collimated

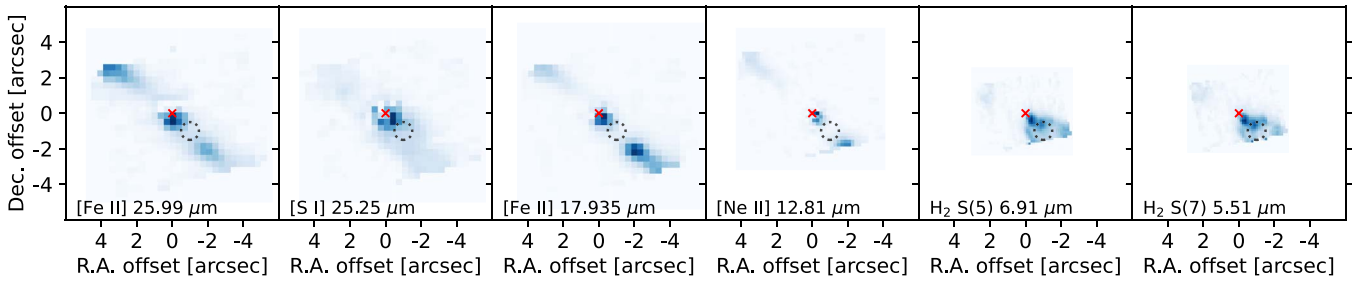


Figure 11. Continuum-subtracted intensity maps of [Fe II] lines at 25.988 and 17.935 μm , [S I] at 25.249 μm , [Ne II] at 12.814 μm , H₂ S(5) and S (7) at 6.910 and 5.511 μm , respectively. The map is calculated from the average intensity within ± 200 km s^{-1} from the rest-frame line centroids. The continuum is calculated from -500 to -300 km s^{-1} . The red cross labels the submillimeter continuum peak position. The dotted circles indicate the extraction aperture for the spectrum shown in Figure 10.

into a jet within the cavity region. In most cases, the ionic lines are spectrally resolved across a few channels, corresponding to a velocity range of ± 200 km s^{-1} . The ionic lines are generally associated with outflows and connected to accretion processes in the central protostar (Watson et al. 2016).

6. Conclusions

It is clear from these first observations of IRAS 15398–3359 that JWST MIRI will transform our understanding of protostellar ice chemistry as well as ice chemistry in all environments. We present detections of previously identified ice species and provide evidence for the possible presence of organic ice species. We also show gaseous emission of warm water and CO, which is often found in warm disks. Other detected emission lines, including H₂, [Fe II], [Ne II], and [S I], appear extended along the outflow direction, tracing a wide-angle outflow cavity and a collimated jet. The MIRI imaging serendipitously captured the southwestern outflow of IRAS 15398–3359, providing us an exquisite view of the outflow structure in the infrared.

The main conclusions of this first analysis of the JWST/MIRI observations of IRAS 15398–3359 are summarized below.

1. A MIRI MRS spectrum of a Class 0 protostar, IRAS 15398–3359, is reported for the first time. The protostar appears as a point source over the full wavelength range at 5–28 μm .
2. The MRS data show rich ice absorption features. Particularly, the ice features between 5 and 8 μm are detected with high S/N, allowing us to search for organic ice species. We robustly identify ice species including H₂O, CO₂, CH₄, NH₃, CH₃OH, H₂CO, and HCOOH. Furthermore, we detect ice absorption features that could imply the presence of NH₄⁺, HCOO⁻, C₂H₅OH, CH₃CHO, and HCOOCH₃. The CH₄ and pure CO₂ ice features appear stronger in the MIRI MRS spectra compared to previous Spitzer studies. Significantly improved spectral resolution could result in deeper absorption, providing accurate constraints on the ice compositions. Stronger absorption could also imply variability in ice column densities.
3. The spectra between 5 and 8 μm have many weaker emission lines. The continuum-subtracted spectra present similar features to those from the synthetic spectra of warm water vapor and CO gas. These emission lines only appear toward the protostar, hinting at warm water vapor and CO gas on small scales possibly on the disk surface.

4. The MIRI imaging captures the blueshifted outflow of IRAS 15398–3359, showing multiple shell-like structures consistent with the molecular outflows seen at submillimeter wavelengths. The infrared outflow has similar length as the submillimeter outflow. The proper motion of the compact shock knot indicates a dynamical time of ~ 150 yr for that ejection.
5. Multiple emission lines are detected in the MRS spectra, including [Fe II], [Ne II], [S I], and H₂. The H₂ S(8) line is the first detection in young protostars.
6. The [Fe II] and [Ne II] emission show a collimated bipolar jet-like structure along the known outflow direction. The emission also highlights a bright knot $\sim 2''$ away from the protostar toward the southwest. The emission of H₂ appears more extended, tracing a wide-angle outflow cavity.

This JWST/MIRI observations of IRAS 15398–3359 show striking details about solid-state features, providing the observational constraints for extensive searches of new ice species and detailed modeling of their abundances. The characterization of gas-phase COMs has progressed significantly in the past decade, in large part due to the maturation of submillimeter interferometry (e.g., ALMA and Northern Extended Millimeter Array). Conversely, observational constraints on the ice-phase COMs are so far mostly from observations using Infrared Space Observatory Short Wavelength Spectrometer and Spitzer/IRS with limited spectral and spatial resolving power and sensitivity. Absorption features of rare organic ice species in low-mass protostars have low contrast and therefore require very high S/N and accurate spectrophotometric calibration to detect. The absorption features between 7 and 8 μm were only detected in high-mass young stellar objects (e.g., W33A) with ISO/SWS, and similar features were only marginally detected with Spitzer in low-mass protostars. Consequently, the composition of organic ices around low-mass protostars has only been weakly constrained until now. With the advent of the JWST and the MIRI spectrograph, the present observations definitively demonstrate that we can now detect and constrain mid-infrared COM ice feature strength at high precision and provide much stronger guidance to models of gas-grain chemistry.

This work is based on observations made with the NASA/ESA/CSA James Webb Space Telescope. The data were obtained from the Mikulski Archive for Space Telescopes at the Space Telescope Science Institute, which is operated by the Association of Universities for Research in Astronomy, Inc.,

under NASA contract NAS 5-03127 for JWST. These observations are associated with JWST GO Cycle 1 program ID 2151. The JWST data used in this paper can be found in MAST doi:[10.17909/wv1n-rf97](https://doi.org/10.17909/wv1n-rf97). Y.-L.Y. acknowledges support from the Virginia Initiative of Cosmic Origins Postdoctoral Fellowship and a Grant-in-Aid from the Ministry of Education, Culture, Sports, Science, and Technology of Japan (22K20389). Y.-L.Y. and N.S. acknowledge support from a Grant-in-Aid from the Ministry of Education, Culture, Sports, Science, and Technology of Japan (20H05845, 20H05844), and a pioneering project in RIKEN (Evolution of Matter in the Universe). L.I.C. acknowledges support from the David and Lucille Packard Foundation, Johnson & Johnson WISTEM2D, and NASA ATP 80NSSC20K0529. Y.-L.Y. thanks J. Terwisscha van Scheltinga for laboratory ice spectra, Y. Okoda for useful discussion on the ALMA observations of the presented source, and S. Zeng and R. Nakatani for the motivation to explore the MIRI imaging products. L.I.C., R.T.G., B.S., J.B.B., C.N.S., K.M.P., and J.D.G. acknowledge support from NASA/STScI GO grant JWST-GO-02151. J.-E.L. and C.-H.K. were supported by the National Research Foundation of Korea (NRF) grant funded by the Korea government (MSIT; grant No. 2021R1A2C1011718). E.v.D. is supported by EU A-ERC grant 101019751 MOLDISK and by the Danish National Research Foundation (grant agreement No. DNRF150, “Inter-Cat”). This research benefited from discussions held with the international team #461 “Provenances of our Solar System’s Relics” (team leaders Maria N. Drozdovskaya and Cyrielle Opitom) at the International Space Science Institute, Bern,

Switzerland. This research has made use of the NASA/IPAC Infrared Science Archive, which is funded by the National Aeronautics and Space Administration and operated by the California Institute of Technology. The National Radio Astronomy Observatory is a facility of the National Science Foundation operated under cooperative agreement by Associated Universities, Inc. This research made use of Photutils, an Astropy package for detection and photometry of astronomical sources (Bradley et al. 2022). This research made use of APLpy, an open-source plotting package for Python (Robitaille & Bressert 2012; Robitaille 2019).

Facilities: JWST, Spitzer, IRSA.

Software: astropy v5.1 (Astropy Collaboration et al. 2013, 2018), jwst (Bushouse et al. 2019), photutils v1.5.0 (Bradley et al. 2022), aplpy v2.1.0 (Robitaille 2019).

Appendix A Characteristics of the Extraction Apertures

The protostar appears pointlike in the MRS spectral cube, showing the Airy pattern most noticeably at the longer wavelengths. Therefore, to extract 1D spectra, we define the aperture in units of the diffraction-limited beam, resulting in variable aperture increasing with wavelength. Because the source is not a perfect point source, we expect the 1D spectrum extracted with a small aperture would lead to missing flux if the emission is more extended due to scattering; the actual beam size may be larger than the diffraction-limited beam size due to the detector scattering at shorter wavelengths. On the other hand, a larger aperture may start to add noise to the 1D

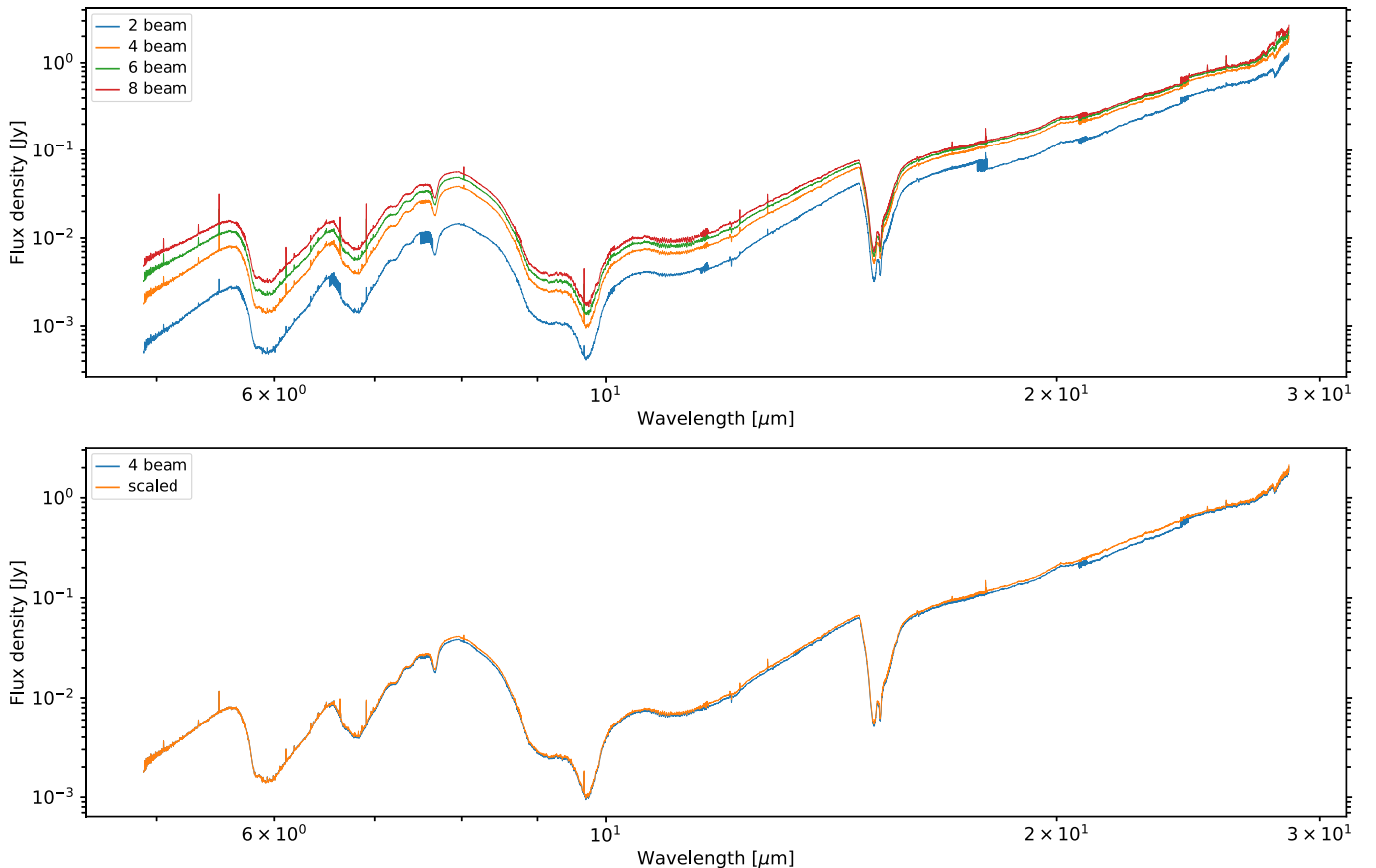


Figure A1. Top: the 1D spectra extracted with aperture sizes of two, four, six, and eight beams without scaling. Bottom: the 1D spectra extracted with a four-beam aperture with and without scaling.

spectrum. The extracted 1D spectra with different aperture sizes demonstrate the aforementioned effects (Figure A1, top). The four-beam aperture extraction results in a good balance between missing flux and noise, which is adopted in this study for extracting the 1D spectrum. The spectrum extracted with a four-beam aperture with the median scaling between subbands (see Section 2) differs from the unscaled spectrum by up to 16% (Figure A1, bottom).

Appendix B Comparison between JWST/MIRI MRS Spectra and Spitzer/IRS Spectra

To check the accuracy of our overall calibration, we compared the MIRI spectra with Spitzer/IRAC aperture photometry, both extracted with a 3'' aperture (Figure B1).

Appropriate aperture corrections were applied to the IRAC aperture photometry (Table 4.8 in IRAC Instrument & Instrument Support Teams 2021). After convolving the MRS spectra with the IRAC 4 filter, the spectrophotometric flux at 8 μm agrees with the IRAC 4 flux. The MRS spectra have limited wavelength coverage that prevents a similar comparison at 5.8 μm . Figure B1 (right) shows the MRS 1D spectra extracted from the protostar compared with the scaled Spitzer/IRS Long-Low (LL1) spectra. The IRS LL1 spectrum matches the long wavelength part of the MRS spectra, making the $\lambda > 30 \mu\text{m}$ in the IRS spectra suitable for baseline fitting.

Figure B2 shows the absorption features in both the MIRI MRS spectrum and the Spitzer/IRS spectra. All features are deeper and much better resolved in the MRS spectra. The apparent shifts in the CO₂ feature (15.2 μm) may be due to the uncertainty in the wavelength solution (Section 2).

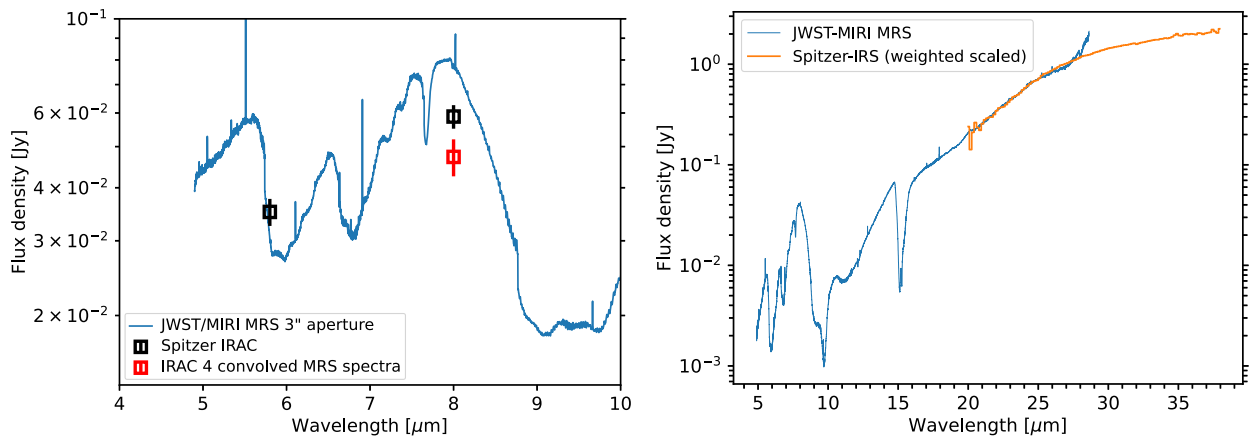


Figure B1. Left: the MIRI MRS spectra compared with Spitzer/IRAC aperture photometry (black). Both data were extracted with a 3'' aperture. The red square shows the MRS spectra convolved with the IRAC 4 filter. The error bars indicate an assumed 10% uncertainty. The aperture photometry is aperture corrected but without color corrections. Right: the MRS 1D spectra along with the scaled Spitzer/IRS spectra at long wavelengths. The scaling factor increases linearly with wavelength to match the wavelength dependency in the extraction aperture of the MRS 1D spectra.

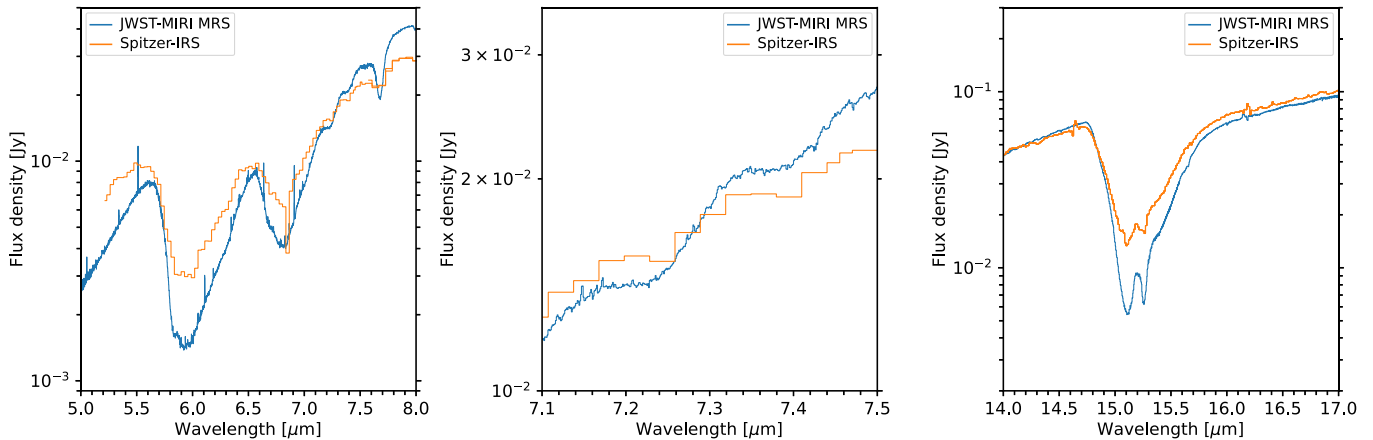


Figure B2. Selected absorption features detected in the MIRI MRS spectra compared with archival Spitzer/IRS spectra.

Appendix C Laboratory Data

Several laboratory absorbance spectra are taken from the Leiden Ice Database for Astrochemistry (LIDA; Rocha et al.

2022) along with others that are collected from individual studies. Table C1 shows the references of ice species included in the composite synthetic ice spectra (Section 3.2). Table C2 lists the absorption features of organic ice species used for the discussion in Section 3.

Table C1
References of Laboratory Spectra

Species	Temperature (K)	References
GCS 3 ^a	...	Kemper et al. (2004)
H ₂ O	15	Öberg et al. (2007)
H ₂ O+CH ₃ OH+CO ₂ +CH ₄ (0.6:0.7:1.0:0.1)	10	Ehrenfreund et al. (1999)
H ₂ O+HCOOH (1:1)	15	Bisschop et al. (2007)
CH ₃ OH	15	Terwisscha van Scheltinga et al. (2018)
CO ₂	15	van Broekhuizen et al. (2006)
CH ₃ CHO	15	Terwisscha van Scheltinga et al. (2018)
CH ₃ CH ₂ OH	15	Terwisscha van Scheltinga et al. (2018)
NH ₃	10	Taban et al. (2003)
H ₂ CO	10	Gerakines et al. (1996)

Note.

^a The GCS 3 spectra are taken from the ice library of ENIIGMA (Rocha et al. 2021).

Table C2
Complex Organic Ice Features Measured in Laboratory

Species	Mode	Peak Position (μm)	Reference
Acetaldehyde (CH ₃ CHO)	CH ₃ rock. + CC stretch. + CCO bend.	8.909	Terwisscha van Scheltinga et al. (2018)
	CH ₃ sym-deform. + CH wag.	7.427	
	CH ₃ deform.	6.995	
	C=O stretch.	5.803	
Ethanol (CH ₃ CH ₂ OH)	CC stretch.	11.36	Terwisscha van Scheltinga et al. (2018)
	CO stretch.	9.514	
	CH ₃ rock.	9.170	
	CH ₂ torsion.	7.842	
	OH deform.	7.518	
	CH ₃ sym-deform.	7.240	
Methyl formate (HCOOCH ₃)	C=O stretch.	5.804	Terwisscha van Scheltinga et al. (2021)
	C–O stretch.	8.256	
	CH ₃ rock.	8.582	
	O–CH ₃ stretch.	10.98	
	OCO deform.	13.02	

Note. The listed features are measured from amorphous ice at 15 K.

ORCID iDs

Yao-Lun Yang  <https://orcid.org/0000-0001-8227-2816>
 Joel D. Green  <https://orcid.org/0000-0003-1665-5709>
 Klaus M. Pontoppidan  <https://orcid.org/0000-0001-7552-1562>
 Jennifer B. Bergner  <https://orcid.org/0000-0002-8716-0482>
 L. Ilseidore Cleeves  <https://orcid.org/0000-0003-2076-8001>
 Neal J. Evans II  <https://orcid.org/0000-0001-5175-1777>
 Robin T. Garrod  <https://orcid.org/0000-0001-7723-8955>
 Mihwa Jin  <https://orcid.org/0000-0002-4801-436X>
 Chul Hwan Kim  <https://orcid.org/0000-0002-2523-3762>
 Jaeyeong Kim  <https://orcid.org/0000-0001-8064-2801>
 Jeong-Eun Lee  <https://orcid.org/0000-0003-3119-2087>
 Nami Sakai  <https://orcid.org/0000-0002-3297-4497>
 Christopher N. Shingledecker  <https://orcid.org/0000-0002-5171-7568>
 Brielle Shope  <https://orcid.org/0000-0003-4147-4125>
 John J. Tobin  <https://orcid.org/0000-0002-6195-0152>
 Ewine F. van Dishoeck  <https://orcid.org/0000-0001-7591-1907>

References

- Aikawa, Y., Furuya, K., Yamamoto, S., & Sakai, N. 2020, *ApJ*, **897**, 110
 Aikawa, Y., Wakelam, V., Garrod, R. T., & Herbst, E. 2008, *ApJ*, **674**, 984
 Altwegg, K., Balsiger, H., & Fuselier, S. A. 2019, *ARA&A*, **57**, 113
 Astropy Collaboration, Price-Whelan, A. M., Sipőcz, B. M., et al. 2018, *AJ*, **156**, 123
 Astropy Collaboration, Robitaille, T. P., Tollerud, E. J., et al. 2013, *A&A*, **558**, A33
 Balucani, N., Ceccarelli, C., & Taquet, V. 2015, *MNRAS*, **449**, L16
 Banzatti, A., Abernathy, K. M., Brittain, S., et al. 2022, *AJ*, **163**, 174
 Belloche, A., Maury, A. J., Maret, S., et al. 2020, *A&A*, **635**, A198
 Bergner, J. B., Martín-Doménech, R., Öberg, K. I., et al. 2019a, *ESC*, **3**, 1564
 Bergner, J. B., Öberg, K. I., & Rajappan, M. 2019b, *ApJ*, **874**, 115
 Bianchi, E., Ceccarelli, C., Codella, C., et al. 2019a, *ESC*, **3**, 2659
 Bianchi, E., Codella, C., Ceccarelli, C., et al. 2019b, *MNRAS*, **483**, 1850
 Bisschop, S. E., Fuchs, G. W., Boogert, A. C. A., van Dishoeck, E. F., & Linnartz, H. 2007, *A&A*, **470**, 749
 Bjerkeli, P., Jørgensen, J. K., & Brinch, C. 2016a, *A&A*, **587**, A145
 Bjerkeli, P., Jørgensen, J. K., Bergin, E. A., et al. 2016b, *A&A*, **595**, A39
 Blake, G. A., Masson, C. R., Phillips, T. G., & Sutton, E. C. 1986, *ApJS*, **60**, 357
 Blake, G. A., Sutton, E. C., Masson, C. R., & Phillips, T. G. 1987, *ApJ*, **315**, 621
 Bockelée-Morvan, D., Lis, D. C., Wink, J. E., et al. 2000, *A&A*, **353**, 1101
 Boogert, A. C. A., Schutte, W. A., Helmich, F. P., Tielens, A. G. G. M., & Wooden, D. H. 1997, *A&A*, **317**, 929
 Boogert, A. C. A., Pontoppidan, K. M., Knez, C., et al. 2008, *ApJ*, **678**, 985
 Bottinelli, S., Ceccarelli, C., Lefloch, B., et al. 2004, *ApJ*, **615**, 354
 Bottinelli, S., Boogert, A. C. A., Bouwman, J., et al. 2010, *ApJ*, **718**, 1100
 Bouvier, M., Ceccarelli, C., López-Sepulcre, A., et al. 2022, *ApJ*, **929**, 10
 Bradley, L., Sipocz, B., Robitaille, T., et al. 2022, *astropy/photutils*: 1.5.0, Zenodo, doi:10.5281/zenodo.6825092
 Bregman, J. D., Hayward, T. L., & Sloan, G. C. 2000, *ApJL*, **544**, L75
 Bushouse, H., Eisenhamer, J., & Davies, J. 2019, in *ASP Conf. Ser.* 523, *Astronomical Data Analysis Software and Systems XXVII*, ed. P. J. Teuben et al. (San Francisco, CA: ASP), 543
 Cazaux, S., Tielens, A. G. G. M., Ceccarelli, C., et al. 2003, *ApJL*, **593**, L51
 Ceccarelli, C. 2004, in *ASP Conf. Ser.* 323, *Star Formation in the Interstellar Medium: In Honor of David Hollenbach*, ed. D. Johnstone et al. (San Francisco, CA: ASP), 195
 Ceccarelli, C., Caselli, P., Herbst, E., Tielens, A., & Caux, E. 2007, in *Protostars and Planets V* (Tucson, AZ: Univ. of Arizona Press), 47
 Ceccarelli, C., Codella, C., Balucani, N., et al. 2022, arXiv:2206.13270
 Chapman, N. L., Lai, S.-P., Mundy, L. G., et al. 2007, *ApJ*, **667**, 288
 Chuang, K. J., Fedoseev, G., Ioppolo, S., van Dishoeck, E. F., & Linnartz, H. 2016, *MNRAS*, **455**, 1702
 De Simone, M., Ceccarelli, C., Codella, C., et al. 2020, *ApJL*, **896**, L3
 Do-Duy, T., Wright, C. M., Fujiyoshi, T., et al. 2020, *MNRAS*, **493**, 4463
 Drozdovskaya, M. N., van Dishoeck, E. F., Rubin, M., Jørgensen, J. K., & Altwegg, K. 2019, *MNRAS*, **490**, 50
 Drozdovskaya, M. N., Walsh, C., Visser, R., Harsono, D., & van Dishoeck, E. F. 2014, *MNRAS*, **445**, 913
 Drozdovskaya, M. N., Walsh, C., Visser, R., Harsono, D., & van Dishoeck, E. F. 2015, *MNRAS*, **451**, 3836
 Ehrenfreund, P., Boogert, A. C. A., Gerakines, P. A., Tielens, A. G. G. M., & van Dishoeck, E. F. 1997, *A&A*, **328**, 649
 Ehrenfreund, P., Kerkhof, O., Schutte, W. A., et al. 1999, *A&A*, **350**, 240
 Escibano, R. M., Muñoz Caro, G. M., Cruz-Díaz, G. A., Rodríguez-Lazcano, Y., & Mate, B. 2013, *PNAS*, **110**, 12899
 Fedoseev, G., Chuang, K. J., Ioppolo, S., et al. 2017, *ApJ*, **842**, 52
 Galli, P. A. B., Bouy, B. H., Olivares, J., et al. 2020, *A&A*, **643**, A148
 Garrod, R. T., Jin, M., Matis, K. A., et al. 2022, *ApJS*, **259**, 1
 Garrod, R. T., Wicidius Weaver, S. L., & Herbst, E. 2008, *ApJ*, **682**, 283
 Gerakines, P. A., Schutte, W. A., & Ehrenfreund, P. 1996, *A&A*, **312**, 289
 Gerakines, P. A., Whittet, D. C. B., Ehrenfreund, P., et al. 1999, *ApJ*, **522**, 357
 Gordon, I. E., Rothman, L., Hargreaves, R., et al. 2022, *JQSRT*, **277**, 107949
 He, J., Emtiaz, S., Boogert, A., & Vidalí, G. 2018, *ApJ*, **869**, 41
 Herbst, E., & van Dishoeck, E. F. 2009, *ARA&A*, **47**, 427
 Herzog, G. J., Brown, J. M., van Dishoeck, E. F., & Pontoppidan, K. M. 2011, *A&A*, **533**, A112
 Heyer, M. H., & Graham, J. A. 1989, *PASP*, **101**, 816
 Hsu, S.-Y., Liu, S.-Y., Liu, T., et al. 2022, *ApJ*, **927**, 218
 Imai, M., Sakai, N., Oya, Y., et al. 2016, *ApJL*, **830**, L37
 IRAC Instrument and Instrument Support Teams 2021, *IRAC Instrument Handbook*, doi:10.26131/IRSA486
 Jacobsen, S. K., Jørgensen, J. K., Di Francesco, J., et al. 2019, *A&A*, **629**, A29
 Jiménez-Serra, I., Vasyunin, A. I., Caselli, P., et al. 2016, *ApJL*, **830**, L6
 Jiménez-Serra, I., Martín-Pintado, J., Rivilla, V. M., et al. 2020, *AsBio*, **20**, 1048
 Jin, M., & Garrod, R. T. 2020, *ApJS*, **249**, 26
 Jørgensen, J. K., Belloche, A., & Garrod, R. T. 2020, *ARA&A*, **58**, 727
 Jørgensen, J. K., Visser, R., Sakai, N., et al. 2013, *ApJL*, **779**, L22
 Keane, J. V., Tielens, A. G. G. M., Boogert, A. C. A., Schutte, W. A., & Whittet, D. C. B. 2001, *A&A*, **376**, 254
 Kemper, F., Vriend, W. J., & Tielens, A. G. G. M. 2004, *ApJ*, **609**, 826
 Kessler-Silacci, J. E., Hillenbrand, L. A., Blake, G. A., & Meyer, M. R. 2005, *ApJ*, **622**, 404
 Kim, H. J., Evans II, N. J., Dunham, M. M., et al. 2011, *ApJ*, **729**, 84
 Lahuis, F., van Dishoeck, E. F., Jørgensen, J. K., Blake, G. A., & Evans, N. J. 2010, *A&A*, **519**, A3
 Lu, Y., Chang, Q., & Aikawa, Y. 2018, *ApJ*, **869**, 165
 Maréchal, Y. 1987, *JChPh*, **87**, 6344
 Nazari, P., Tabone, B., Rosotti, G. P., et al. 2022, *A&A*, **663**, A58
 Nazari, P., van Gelder, M. L., van Dishoeck, E. F., et al. 2021, *A&A*, **650**, A150
 Öberg, K. I., Boogert, A. C. A., Pontoppidan, K. M., et al. 2008, *ApJ*, **678**, 1032
 Öberg, K. I., Boogert, A. C. A., Pontoppidan, K. M., et al. 2011, *ApJ*, **740**, 109
 Öberg, K. I., Fraser, H. J., Boogert, A. C. A., et al. 2007, *A&A*, **462**, 1187
 Okoda, Y., Oya, Y., Sakai, N., et al. 2018, *ApJL*, **864**, L25
 Okoda, Y., Oya, Y., Sakai, N., Watanabe, Y., & Yamamoto, S. 2020, *ApJ*, **900**, 40
 Okoda, Y., Oya, Y., Francis, L., et al. 2021, *ApJ*, **910**, 11
 Oya, Y., Sakai, N., Sakai, T., et al. 2014, *ApJ*, **795**, 152
 Oya, Y., Sakai, N., Watanabe, Y., et al. 2017, *ApJ*, **837**, 174
 Phillips, T. G., van Dishoeck, E. F., & Keene, J. 1992, *ApJ*, **399**, 533
 Pontoppidan, K. M., Fraser, H. J., Dartois, E., et al. 2003, *A&A*, **408**, 981
 Pontoppidan, K. M., Boogert, A. C. A., Fraser, H., et al. 2008, *ApJ*, **678**, 1005
 Puanova, A., Vasyunin, A., Caselli, P., et al. 2022, *ApJ*, **927**, 213
 Qasim, D., Fedoseev, G., Lamberts, T., et al. 2019, *ESC*, **3**, 986
 Quénard, D., Jiménez-Serra, I., Viti, S., Holdship, J., & Coutens, A. 2018, *MNRAS*, **474**, 2796
 Rieke, G. H., Wright, G. S., Böker, T., et al. 2015, *PASP*, **127**, 584
 Rigby, J., Perrin, M., McElwain, M., et al. 2022, arXiv:2207.05632
 Robitaille, T. 2019, *APLpy v2.0: The Astronomical Plotting Library in Python*, Zenodo, doi:10.5281/zenodo.2567476
 Robitaille, T., & Bressert, E. 2012, *APLpy: Astronomical Plotting Library in Python*, Astrophysics Source Code Library, ascl:1208.017
 Rocha, W. R. M., Perotti, G., Kristensen, L. E., & Jørgensen, J. K. 2021, *A&A*, **654**, A158
 Rocha, W. R. M., Rachid, M. G., Olsthoorn, B., et al. 2022, arXiv:2208.12211
 Sakai, N., Sakai, T., Hirota, T., Burton, M., & Yamamoto, S. 2009, *ApJ*, **697**, 769

- Sakai, N., Sakai, T., Hirota, T., & Yamamoto, S. 2008, *ApJ*, **672**, 371
- Salyk, C. 2020, slabspec: Python code for producing LTE slab model molecular spectra, v1.0.0, Zenodo, doi:10.5281/zenodo.4037306
- Salyk, C., Blake, G. A., Boogert, A. C. A., & Brown, J. M. 2011, *ApJ*, **743**, 112
- Salyk, C., Pontoppidan, K. M., Banzatti, A., et al. 2022, *AJ*, **164**, 136
- Schutte, W. A., Allamandola, L. J., & Sandford, S. A. 1993, *Icar*, **104**, 118
- Schutte, W. A., & Khanna, R. K. 2003, *A&A*, **398**, 1049
- Schutte, W. A., Tielens, A. G. G. M., Whittet, D. C. B., et al. 1996, *A&A*, **315**, L333
- Schutte, W. A., Boogert, A. C. A., Tielens, A. G. G. M., et al. 1999, *A&A*, **343**, 966
- Scibelli, S., & Shirley, Y. 2020, *ApJ*, **891**, 73
- Skouteris, D., Balucani, N., Ceccarelli, C., et al. 2018, *ApJ*, **854**, 135
- Soma, T., Sakai, N., Watanabe, Y., & Yamamoto, S. 2018, *ApJ*, **854**, 116
- Spezzano, S., Bizzocchi, L., Caselli, P., Harju, J., & Brünken, S. 2016, *A&A*, **592**, L11
- Sutton, E. C., Blake, G. A., Masson, C. R., & Phillips, T. G. 1985, *ApJS*, **58**, 341
- Taban, I. M., Schutte, W. A., Pontoppidan, K. M., & van Dishoeck, E. F. 2003, *A&A*, **399**, 169
- Taquet, V., Charnley, S. B., & Sipilä, O. 2014, *ApJ*, **791**, 1
- Terwisscha van Scheltinga, J., Ligterink, N. F. W., Boogert, A. C. A., van Dishoeck, E. F., & Linnartz, H. 2018, *A&A*, **611**, A35
- Terwisscha van Scheltinga, J., Marcandalli, G., McClure, M. K., Hogerheijde, M. R., & Linnartz, H. 2021, *A&A*, **651**, A95
- van Broekhuizen, F. A., Groot, I. M. N., Fraser, H. J., van Dishoeck, E. F., & Schlemmer, S. 2006, *A&A*, **451**, 723
- van Dishoeck, E. F., Blake, G. A., Jansen, D. J., & Groesbeck, T. D. 1995, *ApJ*, **447**, 760
- van Gelder, M. L., Tabone, B., Tychoniec, L., et al. 2020, *A&A*, **639**, A87
- Vasyunin, A. I., Caselli, P., Dulieu, F., & Jiménez-Serra, I. 2017, *ApJ*, **842**, 33
- Vazart, F., Ceccarelli, C., Balucani, N., Bianchi, E., & Skouteris, D. 2020, *MNRAS*, **499**, 5547
- Vazzano, M. M., Fernández-López, M., Plunkett, A., et al. 2021, *A&A*, **648**, A41
- Visser, R., Kristensen, L. E., Bruderer, S., et al. 2012, *A&A*, **537**, A55
- Watson, D. M., Calvet, N. P., Fischer, W. J., et al. 2016, *ApJ*, **828**, 52
- Wright, C. M., Do Duy, T., & Lawson, W. 2016, *MNRAS*, **457**, 1593
- Wright, G. S., Wright, D., Goodson, G. B., et al. 2015, *PASP*, **127**, 595
- Yang, Y.-L., Green, J. D., Evans II, N. J., et al. 2018, *ApJ*, **860**, 174
- Yang, Y.-L., Sakai, N., Zhang, Y., et al. 2021, *ApJ*, **910**, 20
- Yen, H.-W., Koch, P. M., Takakuwa, S., et al. 2017, *ApJ*, **834**, 178
- Yıldız, U. A., Kristensen, L. E., van Dishoeck, E. F., et al. 2015, *A&A*, **576**, A109